

Feedback in simulations of disc-galaxy major mergers

T. J. Cox^{1,2}, Patrik Jonsson³, Joel R. Primack¹, and Rachel S. Somerville⁴

¹*Department of Physics, University of California, Santa Cruz, 1156 High St., Santa Cruz, CA, 95064, USA*

²*Harvard-Smithsonian Center for Astrophysics, 60 Garden St., Cambridge, MA 02138, USA; tcoc@cfa.harvard.edu*

³*Department of Astronomy and Astrophysics, University of California, Santa Cruz, 1156 High St., Santa Cruz, CA, 95064, USA*

⁴*Max-Planck-Institut für Astronomie, Königstuhl 17, D-69117 Heidelberg, Germany*

30 June 2018

ABSTRACT

Using hydrodynamic simulations of disk-galaxy major mergers we investigate the star-formation history and remnant properties when various parameterizations of a simple stellar feedback model are implemented. The simulations include radiative cooling, a density-dependent star-formation recipe and a model for feedback from massive stars. The feedback model stores supernova feedback energy within individual gas particles and dissipates this energy on a time-scale specified by two free parameters; τ_{fb} , which sets the dissipative timescale, and n , which sets the effective equation of state in star-forming regions. Via this model, feedback energy can provide pressure support to regions of gas that are thermally cold. Using a self-consistent disk galaxy, modeled after a local Sbc spiral, in both isolated and major-merger simulations, we investigate parameterizations of the feedback model that are selected with respect to the quiescent disk stability. These models produce a range of star formation histories for disks evolved in isolation, or during a major merger, yet all are consistent with the star formation relation found by Kennicutt (1998). We suggest that this result is produced by the adopted recipe for star formation and is not a byproduct of the feedback model. All major mergers produce a population of new stars that is highly centrally concentrated, demonstrating a distinct break in the $r^{1/4}$ surface density profile, consistent with previous findings. The half-mass radius and one-dimensional velocity dispersion are affected by the feedback model used. In tests with up to an order of magnitude higher resolution, the star formation history is nearly identical, suggesting that we have achieved a numerically converged star formation history. Finally, we compare our results to those of previous simulations of star formation in disk-galaxy major mergers, addressing the effects of star-formation normalization, the version of smoothed particle hydrodynamics (SPH) employed, and assumptions about the interstellar medium. We conclude by suggesting several methods by which future studies may better constrain feedback models.

Key words: galaxies: interactions – galaxies: evolution – galaxies: starburst – galaxies: formation – methods: numerical.

1 INTRODUCTION

It is commonly assumed that galaxy interactions trigger powerful bursts of star formation. This assumption is supported by a variety of observational data which links morphologically disturbed or outright merging galaxies to enhanced levels of star formation (e.g., Larson & Tinsley 1978; Joseph & Wright 1985; Kennicutt et al. 1987; Barton Gillespie et al. 2003; Lambas et al. 2003; Nikolic et al. 2004). In fact, the most vigorously star-forming galaxies in the local universe, the ultra-luminous infrared galaxies (ULIRGs), are nearly all mergers (Sanders & Mirabel 1996; Borne et al. 2000).

Indeed, one of the fundamental assumptions of many galaxy-formation models is the efficient conversion of cold gas into new stars whenever two galaxies merge. These assumptions appear to be necessary in order to reproduce the abundance of Lyman-Break (Somerville, Primack & Faber 2001) and submillimeter (Guiderdoni et al. 1998; Baugh et al. 2005) galaxies.

The numerical simulations run to-date have supported the theory that disk-galaxy mergers yield a burst of star formation. The earliest work established that galaxy mergers can concentrate a large amount of gas in the central regions of the remnant (Negroponete & White 1983; Hernquist 1989;

Barnes & Hernquist 1991, 1996). Later, by including simple recipes to capture star formation and kinetic feedback from massive stars, Mihos & Hernquist (1994c, 1996, hereafter MH96) produced the first quantitative results for the star formation induced during a major merger. These authors found that mergers between two equal mass gas-rich galaxies, so-called major mergers, trigger star formation at every close passage of the galactic nuclei, culminating in a burst at the final merger. In total, these starbursts convert $\sim 80\%$ of the original gas mass into stars, an efficiency apparently independent of galaxy orientation or the presence of a spheroidal bulge in the primary disk galaxy.

Subsequent work has become more ambitious. Springel (2000, hereafter S00) employed a slightly more elaborate treatment of the interstellar medium (ISM) by accurately treating gas heating and cooling. More recently, simulations have included shock-induced star formation (Barnes 2004) and accreting black holes (Springel, Di Matteo & Hernquist 2005b). While all of these studies have supported the fact that major mergers induce star formation, it has become clear that the star-formation efficiency is highly dependent upon the star formation and feedback assumptions. Because we lack a detailed theory of star formation and the influence young stars have on their surroundings, there are no clear means to include these physical processes in numerical simulations. The typical approach is to formulate physically or observationally motivated recipes whose impact is controlled by one or more free parameters. This methodology is also motivated by the finite numerical resolution achievable. Current state-of-the-art numerical simulations evolve individual fluid elements which each represent $\sim 10^5 M_{\odot}$ and 100 pc. As an example, star formation on kpc scales is observationally found to trace the gas density in what is known as the Schmidt law (Schmidt 1959; Kennicutt 1998). Motivated by this relation, simulations can employ a recipe that converts gas to stars based on the local gas density. In this sense, a simulation can capture the sub-resolution star formation averaged over scales that are numerically resolved. Unfortunately, there exists no clear analog to the Schmidt-law for the effects of massive stellar winds and supernovae.

Effective parameterizations for stellar feedback have been included in numerical simulations for the past decade. The first attempts used “thermal feedback,” in which energy released by supernovae simply increases the thermal energy of the gas (Katz 1992). Subsequent tests have yielded one of the most robust results regarding feedback: thermal feedback is ineffective at regulating star formation due to the short cooling times (and rapid thermal energy loss) in dense star-forming regions (S00; Navarro & White 1993; Mihos & Hernquist 1994b). Extensions of thermal feedback, in which a fraction of the supernova energy is imparted as kinetic energy to nearby gas (Navarro & White 1993; Mihos & Hernquist 1994b), have proved effective at producing stable, constantly star-forming disk galaxies, yet have the negative property that their implementations are resolution dependent (S00) and they have difficulty stabilizing disks with a large gas fraction. Beyond this kinetic feedback, most other recipes have looked to prevent the efficient radiation of feedback energy. Gerritsen & Icke (1997) used UV radiation from young stars to offset efficient cooling, S00 created a turbulent reservoir that retained feedback energy for a set time-scale, and Thacker & Couchman

(2001) simply inhibited cooling for 30 Myr subsequent to the injection of feedback energy (see Thacker & Couchman 2000 and Kay et al. 2002 for a comparison of various feedback methods). More recently, methods have been developed to model the multiphase nature of the ISM (Yepes et al. 1997; Hultman & Pharasyn 1999; Semelin & Combes 2002; Marri & White 2003; Springel & Hernquist 2003) and the effects that supernovae blastwaves may have on the ISM (Stinson et al. 2006). While each of the above models has advantages and disadvantages, many of these methods choose to regulate star formation in an equivalent manner: by using feedback energy to effectively pressurize the ISM in star-forming regions.

In this paper, we address the issue of supernova feedback in more detail. Using a generalization of the star-formation and feedback model of S00, we explore a range of parameters and determine how the resulting starburst is affected. This is a slightly different approach than previous work, in that instead of physically motivating a specific feedback model, we attempt to understand how assumed feedback parameters affect star formation. Both the overall efficiency of feedback and its dependence on gas density through an effective equation of state are explored. One of our long-term goals is to uniquely determine a single parameter set, or feedback model, which will be used for a large series of major- and minor-merger simulations. Unfortunately, it is difficult to define a checklist against which each model can be measured, and hence it is difficult for us to endorse one model as significantly better than any other. We can, however, identify trends that are present in our various models and use these to guide parameter exploration in future work.

An important aspect of the work presented here will be to detail how assumptions made by MH96 and S00 affected their merger-induced starbursts. Even though these papers arrived at similar conclusions, the galaxy models, temperature and equation of state of the ISM, implementation of feedback, and N-body/smoothed particle hydrodynamics (SPH) code were all different. This last point is particularly relevant as the conservation of energy and entropy depends on the formulation of SPH as well as the numerical resolution (Hernquist 1993b; Thacker et al. 2000; Springel & Hernquist 2002). In general, all versions of SPH converge to an identical solution for high resolution, but can be quite different at low resolution. This result has recently motivated Springel & Hernquist (2002) to develop a new formulation of SPH which manifestly conserves both energy and entropy, when appropriate. We will investigate what effects this new version of SPH has and how this compares to older formulations of SPH. We also address the numerical convergence of our simulations by performing mergers with up to ten times the resolution. In additional tests, we vary the assumed gas metallicity and star-formation efficiency and determine the resultant star formation.

In our study of the star-formation response to different parameterizations of feedback, we find that the properties of the merger remnants are also affected. This is significant because mergers between spiral galaxies are considered the most likely mechanism to form galactic spheroids. This “merger hypothesis” (Toomre & Toomre 1972; Toomre 1977) is generally supported by simulations (Hernquist 1992, 1993c; Naab & Burkert 2003, S00), and here we show that

details of the feedback model will affect the ability to test the merger hypothesis. We reserve an exhaustive study of the merger remnants to future work, but the variation of feedback parameters alters the basic properties of the merger remnant, and we document these effects here.

In short, we address the following issues in this work:

- (i) How does the star-formation rate and the global gas consumption depend upon the feedback model and feedback parameters?
- (ii) Is the merger remnant affected by the choice of feedback parameters?
- (iii) Are our models consistent with previous simulations of disk-galaxy interactions? Does using a modified version of SPH that manifestly conserves both energy and entropy, when appropriate, change the star-formation evolution?

This paper is designed to be one in a series which compiles the star-formation and remnant properties for a large number of galaxy merger simulations. Prior work has analyzed the kinematics of the merger remnants (Dekel et al. 2005), the influence of dust on the observed properties of the interacting system (Jonsson et al. 2006), the shapes of the stellar and dark matter remnants (Novak et al. 2006), and the dissipative origin of elliptical galaxies (Dekel & Cox 2006). Future work will investigate the star formation induced during mergers between unequal mass galaxies (Cox et al., in preparation), propose a model that predicts the properties of merger remnants (Covington et al., in preparation), and compare the simulations to observed samples of interacting and merging galaxies using non-parametric morphological classification systems (Lotz et al., in preparation).

We organize this paper as follows. To begin, §2 details the numerical techniques and the physical ingredients implemented into the simulations, and §3 introduces a disk galaxy which will be used to investigate our feedback models. This disk galaxy is simulated in isolation in §3.2 and during a major merger in §4. §4 also shows the star-formation history (§4.1) and takes a brief look at the properties of the merger remnant (§4.4). We discuss our results in §5, including a resolution study (§5.1), a comparison to previous work (§5.2), and the effects of varying the ISM metallicity (§5.3). Finally, §6 provides some concluding remarks and a prospectus for future work using the techniques we have developed in this paper.

2 NUMERICAL SIMULATIONS

All numerical simulations performed in this work use the N-Body/SPH code GADGET (Springel, Yoshida & White 2001). Specifically, we use a variant of the publically available version which has the “conservative entropy” version of SPH (Springel & Hernquist 2002), and additional routines that track the radiative cooling of gas and star formation. This version of GADGET was obtained from Volker Springel in 2001. In addition, we implemented several new features ourselves; stellar feedback, metallicity-dependent cooling, and the ability of each gas particle to spawn multiple new stellar particles. The following subsections describe in more detail the physical processes included in our simulations.

2.1 Cooling

Due to radiative cooling, baryons fall into the centers of dark-matter halos and achieve the cold, dense environment conducive to the formation of stars. The radiative cooling rate Λ_{net} is computed as described in Katz, Weinberg & Hernquist (1996), where the gas is treated as a primordial plasma and the ionization states of H and He are explicitly tracked under the assumption of collisional ionization equilibrium. In practice, the radiative cooling rate Λ_{net} then simply a function of the local gas density ρ_{gas} and internal energy per unit mass u . However, the radiative cooling of astrophysical plasmas also highly dependent upon the gas metallicity, we also ran merger simulations using the tabulated cooling curves of Sutherland & Dopita (1993), which allow for a range of metallicities. The results of these simulations are presented in §5.3. In all simulations the spatial and temporal changes in metallicity are ignored, although we keep track of these for use in radiative transfer calculations through the dusty ISM (Jonsson et al. 2006; Jonsson 2006). Lastly, we remind the reader that, without adiabatic processes, the radiative cooling described here, in which molecular cooling is neglected, effectively sets the minimum gas temperature to 10^4K .

2.2 Star Formation

All numerical simulations presented here include star formation. Star formation is assumed to be proportional to the local gas density and inversely proportional to the local dynamical time-scale

$$\frac{d\rho_{\star}}{dt} = c_{\star} \frac{\rho_{\text{gas}}}{t_{\text{dyn}}}, \quad (1)$$

where c_{\star} is a free parameter determining the efficiency of star formation, and $t_{\text{dyn}} = (4\pi G \rho_{\text{gas}})^{-1/2}$. This star-formation recipe mirrors the approach commonly implemented in numerical simulations (MH96; S00; Katz 1992; Springel & Hernquist 2003), however we will briefly revisit this in § 5.2.3.

The star-formation prescription set forth by Equation (1) was originally motivated by star-forming regions in our own galaxy (Schmidt 1959) but has been shown to hold in a wide range of environments. The observational work of Kennicutt (1998) has shown that, on kpc scales, the aperture-averaged star-formation rate per unit area is correlated to the gas surface density. This relation is empirically determined to be

$$\Sigma_{\text{SFR}} = (2.5 \pm 0.7) \times 10^{-4} \left(\frac{\Sigma_{\text{gas}}}{\text{M}_{\odot} \text{pc}^{-2}} \right)^{1.4 \pm 0.15} \frac{\text{M}_{\odot}}{\text{yr kpc}^2}, \quad (2)$$

and will be referred to as the “Kennicutt law” throughout the remainder of this paper. While the index 1.4 resembles the $\dot{\rho}_{\star} \sim \rho_{\text{gas}}^{1.5}$ implied by Equation (1), we must admit that it is not immediately clear that the three-dimensional Schmidt-law, based upon the gas volume density, should be equivalent to the empirical two-dimensional Kennicutt-law, based upon the gas surface density. Nevertheless, the simulations do obey (2), as shown in §3.3

Kennicutt (1998) found the existence of a surface density threshold at $\sim 10 \text{ M}_{\odot} \text{ pc}^{-2}$, below which star formation dramatically drops (Kennicutt 1998; Martin & Kennicutt

2001). To capture this effect in our numerical simulations, we introduce a volume-density threshold, ρ_{th} . Gas which has a density larger than ρ_{th} is eligible to form stars at a rate given by Equation (1). We adopt $\rho_{\text{th}} = 0.0171 \text{ M}_{\odot} \text{ pc}^{-3}$, a value similar to that used in S00 (MH96 did not include such a density threshold) and confirmed to reproduce the observational suppression of star formation below $10 \text{ M}_{\odot} \text{ pc}^{-2}$. Interestingly, Equation (2) also appears to hold for azimuthally-averaged gas densities and star-formation rates in individual galaxies, although the scatter seems to be much larger and the slope shallower (Martin & Kennicutt 2001; Wong & Blitz 2002).

Our implementation of star formation is fully determined by the one free parameter in Equation (1), c_{\star} . To help us select a numerical value for c_{\star} we define the characteristic time-scale for star formation as

$$t_{\star} = \frac{\rho_{\text{gas}}}{\dot{\rho}_{\star}} = \frac{t_{\text{dyn}}}{c_{\star}}. \quad (3)$$

Equation (3) relates the star-formation time-scale to the dynamical time by our one free parameter c_{\star} . Both time-scales become short at high densities. Observations indicate that the median gas consumption time-scale is much longer than the dynamical time-scale, suggesting that $c_{\star} \ll 1$ (Kennicutt 1998). After experimenting with various values for c_{\star} (see §5.2) we found that 0.03 provided a good fit to Equation (2), although we caution that the observational scatter is quite large - almost an order of magnitude higher or lower. Hence there could be a range of allowed values for c_{\star} , all consistent with the Kennicutt law. Our value of $c_{\star} = 0.03$ fixes the time-scale for star formation to be 1.1 gigayear (Gyr) at ρ_{th} . Many previous studies also include star formation via Equation (1). These works use a wide range of star-formation efficiencies that are both higher (Katz 1992; Navarro & White 1993; Kobayashi 2004; Governato et al. 2004; Kawata & Gibson 2005) and lower (MH96; S00; Sommer-Larsen, Götz & Portinari 2003; Springel & Hernquist 2003) than ours. In addition, several authors investigated a range of values for c_{\star} (Bekki & Shioya 1998; Thacker & Couchman 2000) as we do in §5.2, or use a hybrid model where c_{\star} can change with redshift or environment (Sommer-Larsen et al. 2003; Okamoto et al. 2005).

Very little is known about the requisite conditions enabling star formation to occur. Previous simulations (see e.g., Katz 1992; Kravtsov 2003; Governato et al. 2004) have included star formation criteria such as gas convergence, Jeans instability, and temperature thresholds. With the resolution of current simulations, where individual particles represent $\geq 10^5 \text{ M}_{\odot}$ of gas, it is not clear that gas convergence should be required. The Jeans criterion is dependent on the numerical smoothing length, and hence has the undesirable behavior that it is a function of numerical parameters. Finally, as mentioned above, our treatment of cooling sets the minimum gas temperature at 10^4 K , thus we do not expect gas to approach physically reasonable temperatures for star formation ($\leq 50 \text{ K}$). For these reasons we have not included any of the above criteria in the work presented here.

As gas is converted into stars at the rate dictated by Equation (1), one must decide how to handle the newly formed stellar mass. Since it is not computationally feasible to form individual solar-mass particles, numerical sim-

ulations commonly treat SPH particles as “hybrid” particles, representing both gas and new stellar material (e.g. Mihos & Hernquist 1994b). While this procedure is relatively simple to implement, it has the disadvantage that new stellar material is dynamically coupled to the gas.

An alternative approach, suggested by several authors (e.g., Katz 1992; Springel & Hernquist 2003; Bottema 2003), is to treat star formation as a stochastic process. Under this assumption each gas particle spawns a specified number N_g of equal-mass star particles. Then, if each gas particle forms a new star particle according to the probability

$$P = N_g (1 - e^{-dt/t_{\star}}), \quad (4)$$

the stochastic star-formation rate will equate to the designed continuous star-formation rate when averaged over the entire simulation time. We follow the above authors when implementing this procedure, and thus at each timestep actively star-forming gas particles draw a random number between zero and one. If this random number is less than P , a new collisionless particle, of mass m_{gas}/N_g , is created. We note that m_{gas} is the original gas particle mass and that the SPH particle mass decreases as individual star particles are generated. For the majority of the simulations used in this work, we select $N_g = 2$, although we have tried varying N_g up to 10 and found little difference in the results (see the end of §4.4 for details).

Throughout this work stars formed during the simulation will be called “new”, as opposed to “young”, stars. We make this choice because at any point during the simulation there exists a mixture of newly generated stars which have a distribution of stellar ages. While many of these particles are part of a young stellar population, a small percentage will have ages of several gigayears by the time the simulation is complete.

2.3 Metal Enrichment

Although it is not part of the analysis in the present paper, we have also included metal enrichment owing to stellar winds and supernovae ejecta. The enrichment, which assumes a yield of 0.02 per solar mass of stars formed and instantaneous recycling, is performed in a continuous fashion, based upon the instantaneous star-formation rate provided by Equation (1). The star-formation rate is calculated for each particle and metals are recycled within the same particle, i.e., metals are not distributed among neighboring particles nor is the diffusion of metals considered. These metals are carried by each gas particle and subsequent generations of new star particles adopt the metallicity of the parent gas particle at the time when they are born. Under these assumptions, the metallicity of individual gas particles can only increase with time. However, once the gas particle is fully transformed into stars, these metals are forever locked in the stellar component. We intend to implement a more realistic approach where star particles return a fraction of their mass and metals back to the interstellar medium in the future (see, e.g., Mosconi et al. 2001; Tornatore et al. 2004; Okamoto et al. 2005; Scannapieco et al. 2006, 2005). Finally, as noted in § 2.1, even though we track the metallicity of the gaseous component, this information does not affect the cooling rate.

2.4 Feedback

As discussed in the introduction, many of the methods by which feedback from young stars is incorporated into numerical simulations involve artificially pressurizing gas in high-density, star-forming regions. Within SPH, where particles represent fluid elements, this pressurization is implemented on a particle by particle basis. This general approach is also used for the present study but, because there exists no clear theoretical understanding of how feedback pressurization should depend on the physical state of the star-forming regions, we instead adopt a general formalism and investigate the star-formation response to a variety of different parameter choices.

As the starting point for our exploration into feedback, we begin by adopting the feedback model put forth by S00. The relative simplicity of this model and the ease with which it can be implemented into GADGET motivate this choice. Within this model, and adopting the nomenclature of S00, gas is assumed to consist of two energy reservoirs. One, the standard thermal energy u , can radiatively cool at a rate given by Λ_{net} . The second, q , is an “ad-hoc” feedback reservoir. The pressure of this medium is then calculated as

$$P_{\text{eff}} = (\gamma - 1)(u + q)\rho, \quad (5)$$

where ρ is the gas density (the gas subscript is henceforth dropped), and γ is 5/3, consistent with the assumption of a monatomic ideal gas. Equation (5) demonstrates that regions which are thermally cold, possibly because the density is such that cooling is very efficient, can be pressure supported if the feedback reservoir $q \gg u$.

Feedback energy is assumed to come from core collapse supernovae and is calculated in a manner similar to Navarro & White (1993). New stars form with a power-law initial mass function of slope -1.5 between 0.1 and 40 M_{\odot} , and every star above 8 M_{\odot} goes supernova releasing 10^{51} ergs of energy. The short lifetime of these high-mass stars is ignored and supernova energy is instantly returned to the system. We have investigated the effects of including realistic delays in supernova feedback, but it made little difference to the results reported here. We also investigated a limited range of excursions from the initial-mass function and high-mass cutoff listed above. In practice, though, these changes can be compensated with variations in our star formation or feedback free parameters and we do not consider this further. The supernova feedback energy per solar mass of newly formed stars ϵ_{SN} is assumed to be first released into the feedback reservoir q , i.e.

$$\left(\frac{dq}{dt}\right)_{\text{feedback}} = \epsilon_{\text{SN}} \frac{1}{\rho} \frac{d\rho_{\star}}{dt}. \quad (6)$$

The feedback reservoir subsequently thermalizes its energy as

$$\left(\frac{dq}{dt}\right)_{\text{thermalize}} = -\left(\frac{du}{dt}\right)_{\text{thermalize}} = -f(\rho)q \quad (7)$$

where $f(\rho)$ parameterizes the efficiency of thermalization.

The original work of S00 chose $f(\rho) = \beta/\sqrt{\rho}$, i.e., the thermalization of feedback energy is slower in high-density regions. For star-forming gas whose pressure is determined by the feedback reservoir, this choice results in a “stiff” equation of state $P \sim \rho^2$. S00 provided two motivating factors for this model. First, a self-gravitating sheet of gas with

this equation of state has a vertical scale height that is independent of surface density, similar to observations. Second, if the star-formation law is given by Equation (1), then this same self-gravitating sheet has a star formation rate per unit area Σ_{SFR} that scales as the gas surface mass density σ to the 1.5 power, i.e., $\Sigma_{\text{SFR}} \propto \sigma^{1.5}$. In other words, the star formation expected for an isolated disk manifestly scales in a similar fashion to the observed Kennicutt law (Equation 2).

While the formulation set forth by S00 was quite successful at regulating star formation in both isolated and merging galaxies and, as designed, reproduced the observed star formation laws, there are several reasons to explore alternative formulations. First, it is not clear that all observations have converged on vertical scale heights of disk galaxies that are independent of radius. Second, the observed star-formation law holds in physical environments, such as the centers of spiral galaxies and in merging galaxies, that are very different from isolated disks. Thus, while the S00 equation of state naturally predicts isolated disks that follow Kennicutt, this may be a necessary, but not a sufficient condition. Lastly, a quick survey of the literature returns a number of alternate formations of feedback which do not lead to the S00 equation of state yet are still able to regulate star formation consistent with the Kennicutt relation (see e.g., Springel et al. 2005b).

For these reasons, we depart from S00 at this point and assume $f(\rho)$ is a general power-law function of density, i.e.,

$$f(\rho) = \frac{1}{\tau_{\text{fb}}} \begin{cases} \left(\frac{\rho}{\rho_{\text{th}}}\right)^{(1-n)/2}, & \text{for } \rho > \rho_{\text{th}} \\ \left(\frac{\rho}{\rho_{\text{th}}}\right)^{-1/2}, & \text{for } \rho < \rho_{\text{th}} \end{cases} \quad (8)$$

where ρ_{th} is the critical density for star formation and we have introduced two free parameters: τ_{fb} , the timescale with which feedback energy is dissipated (and hence the efficiency of the feedback), and n which sets the polytropic index. The power-law below ρ_{th} is fixed at $n = 2$ to ensure that the feedback dissipation timescale gets shorter for low-density gas. We note that setting $\tau_{\text{fb}} = \sqrt{\rho_{\text{th}}}/\beta$ and $n = 2$ transforms our model to the S00 model.

In order to gain some insight into our model, as well as facilitate the selection of parameters to explore, we next cast our model in terms of an effective temperature and pressure in star-forming regions. Specifically, we consider a region of gas where the adiabatic energy changes are negligible, but which is also at a density greater than ρ_{th} and hence is actively forming stars. Under these conditions the feedback reservoir will reach a steady state in which the energy input due to supernovae (6) equals the energy lost to thermalization (7), which is subsequently radiated away, viz.,

$$q = \epsilon_{\text{SN}} \frac{c_{\star}}{t_{\text{dyn}}} \frac{1}{f(\rho)} = \epsilon_{\text{SN}} c_{\star} \left(\frac{\tau_{\text{fb}}}{t_{\text{dyn}}}\right) \left(\frac{\rho}{\rho_{\text{th}}}\right)^{(n-1)/2}. \quad (9)$$

This results in star-forming regions that have an effective temperature and pressure given by

$$T_{\text{eff}} \simeq \frac{(\gamma - 1)\bar{\mu}}{k} \epsilon_{\text{SN}} c_{\star} \left(\frac{\tau_{\text{fb}}}{t_{\text{dyn}}}\right) \left(\frac{\rho}{\rho_{\text{th}}}\right)^{(n-1)/2}, \quad (10)$$

and

$$P_{\text{eff}} \simeq (\gamma - 1)\epsilon_{\text{SN}} c_{\star} \left(\frac{\tau_{\text{fb}}}{t_{\text{dyn}}}\right) \left[\frac{\rho^{(n+1)/2}}{\rho_{\text{th}}^{(n-1)/2}}\right], \quad (11)$$

Table 1. Star-formation and feedback parameter sets used in either isolated galaxy or major-merger simulations, or both. c_* is the star-formation efficiency and n the density dependence of the feedback energy thermalization timescale. τ_{fb} is the thermalization timescale, and T_{eff} the effective temperature, in Kelvin, at the threshold density for star formation ρ_{th} . S00 used the same feedback parameters as our $n = 2$ “low-feedback” model, but a lower star-formation efficiency which is below the Kennicutt value.

Model	c_*	n	τ_{fb} (Myr)	T_{eff} at ρ_{th} (K)
S00	0.004	2	0.83	3.5×10^3
<i>low</i>	0.03	0,1,2	0.83	2.6×10^4
<i>medium</i>	0.03	0,1,2	8.3	2.6×10^5
<i>high</i>	0.03	0,1,2	82.7	2.6×10^6

where $\bar{\mu}$ is the mean molecular weight, and k is Boltzmann’s constant.

As mentioned previously, and shown explicitly by Equation (11), n fixes the polytropic index, i.e., the power-law dependence of pressure on gas density $P \propto \rho^{1+n/2}$ (remember that $t_{\text{dyn}} \propto \rho^{-1/2}$). When $n = 0$, the pressure increases linearly with the density, as in an isothermal gas. When $n > 0$, the pressure increases faster than linear, and in this case the gas has a “stiff” equation of state. In this work we will investigate three choices of n : 0, 1 and 2, thus from isothermal to the same $n = 2$ as investigated in S00. While the present study assumes that n is a constant, there is no reason why n could not be a function of gas density. In fact, this is the case in a recent study by Springel et al. (2005b) where their “multi-phase” model results in $n = 2.8$ near ρ_{th} and then gradually softens to $n = 0.7$ at higher densities.

To minimize the effects of the feedback reservoir q in low-density regions, i.e. below the critical threshold for star formation, $f(\rho)$ is fixed to $\tau_{\text{fb}}\rho^{-1/2}$ (i.e., $n = 2$) for $\rho < \rho_{\text{th}}$. The coefficient τ_{fb} ensures that $f(\rho)$ is continuous at ρ_{th} .

The numerical implementation of these star formation and feedback processes is handled in a continuous fashion on a particle-by-particle basis. At each timestep, active gas particles can form stars and instantaneously deposit energy into the ISM. Thus, Equations (6) and (7) become source terms in the standard hydrodynamic equations that are evolved within GADGET.

2.5 Parameter Sets

The star-formation and feedback model presented in the previous sections has three free parameters: c_* , controlling the efficiency of star formation, τ_{fb} , determining the timescale of feedback thermalization, and n , specifying the feedback density dependence, or, as Equation (11) demonstrates, the equation of state. While the star-formation efficiency c_* was fixed in § 2.2, τ_{fb} and n are essentially free parameters.

The approach of the work presented here is to survey a range of feedback parameters which sample, but not exhaust, viable possibilities. Unfortunately, it is unclear how to judge the viability of feedback parameters. One possibility that has been frequently used in the literature is to require that the feedback be sufficient to stabilize the gaseous disk of a quiescent spiral galaxy against dynamic instabili-

ties. This appears to be a zeroth-order requirement because observed spiral galaxies *are* dynamically stable. While this procedure is well defined, it does not generally yield a unique parameter set, but rather sets a minimum amount of feedback necessary to stabilize a specific galaxy model. Galaxy models that have high gas fractions, high baryon fractions, and slowly rising rotation curves will be more susceptible to disk instabilities and thus require more feedback.

In the current paper, we will also use the quiescent disk galaxy stability as a tool to investigate parameter choices. However, the model disk galaxy we use is designed to represent a Sbc Hubble-type galaxy (this will be introduced in the following section), and thus is a large, gas-rich spiral that represents one of the most gravitationally unstable galaxies observed. Since Sbc spirals *are* stable, it seems reasonable to require that any plausible feedback model will need to stabilize our Sbc model. In practice, the feedback model may be more stable, and thus we will investigate a range of parameter sets and attempt to understand their consequences.

In order to define a reference feedback timescale τ_{fb} , we look at the stability of our isolated galaxy model gas disk as measured by the Toomre Q parameter (Binney & Tremaine 1987, eq. 6-49), i.e.,

$$Q = \frac{c_s \kappa}{\pi G \Sigma_{\text{gas}}}, \quad (12)$$

where $c_s^2 = \gamma P \rho^{-1}$ is the sound speed, κ the epicyclic frequency, and Σ_{gas} the gas surface density. For our model, the pressure of star-forming gas, and hence its sound speed, is approximated by Equation (11). We also note that observations suggest that most disk galaxies reside very close to $Q \sim 1$ (Martin & Kennicutt 2001; Wong & Blitz 2002). Thus, by inserting (11) into (12), and setting $Q = 1$ we arrive at an expression for the feedback efficiency

$$\tau_{\text{fb}} = \frac{t_{\text{dyn}}}{\gamma(\gamma - 1)\epsilon_{\text{SN}}c_*} \left(\frac{\Sigma_{\text{gas}}\pi G}{\kappa} \right)^2 \left(\frac{\rho}{\rho_{\text{th}}} \right)^{(1-n)/2}. \quad (13)$$

Thus, via Equation (13), τ_{fb} can be determined from the star-formation efficiency c_* , the feedback density dependence n , the dynamical time at a specified density and a disk-galaxy model which specifies κ and Σ . Equation (13) has the nice property that if it is evaluated at $\rho = \rho_{\text{th}}$, as we will do here, then the dependence on n is removed. In practice, both κ and Σ are functions of disk radius, but their ratio reaches a minimum at approximately twice the exponential disk scale length and we adopt this value for use in Equation (13).

We will label the $Q = 1$ case as the “medium” parameter set and use this as a reference for explorations to a superstable “high” parameter set and an unstable “low” parameter set, which are ten times higher and lower, respectively, and should maintain the disk at $Q \simeq 3$ and $Q \simeq 0.3$. These values of τ_{fb} serve to sample the range of plausible feedback efficiencies, and our model disk galaxy will be simulated in isolation and during a major merger for each parameter set. Table 1 lists the three values of τ_{fb} as well as the labels that will be used to reference each parameter set from this point forward.

Table 2. Properties of the Sbc disk-galaxy model used in this work. M_{vir} is the virial mass, including dark matter and baryons. The dark-matter halo has a NFW profile with a concentration c and spin parameter λ , before this is contracted due to the presence of the baryons. The baryonic mass is distributed into one of three components: an exponential stellar disk, an exponential gas disk, or a stellar bulge. The mass fraction of each baryonic component is given by m_d , m_g , and m_b . R_d is the stellar disk exponential scale length and z_0 is the vertical scale height. The gas disk has a scale length α times R_d . Both gas and stellar disks are rotationally supported with angular momentum j_d and j_g given in terms of the total angular momentum. Finally, the bulge has a spherical exponential distribution with scale radius R_b .

Sbc	
Virial Mass, M_{vir}	$8.12 \times 10^{11} M_{\odot}$
Concentration, $c=R_{\text{vir}}/r_s$	11
Spin Parameter, λ	0.05
Disk Mass Fraction, m_d	0.048
Radial Disk Scale Length, R_d	5.5 kpc
Vertical Scale Height, z_0	1.0 kpc
Stellar Disk Spin Fraction, j_d	0.058
Gas Mass Fraction, m_g	0.065
Gas Scale Length Multiplier, α	3.0
Gas Spin Fraction, j_g	0.219
Bulge Mass Fraction, m_b	0.012
Bulge 3D Scale Length, R_b	0.45 kpc
N_{halo}	100,000
N_{disk}	30,000
N_{gas}	30,000
N_{bulge}	10,000

3 ISOLATED DISK GALAXIES

3.1 The Basics of Model Disk Galaxies

In this section we describe the basic ingredients of our model disk galaxy. In general, these models are similar to those described in Hernquist (1993a), Mihos & Hernquist (1996), Springel & White (1999), and S00, as they contain a stellar and gaseous disk, which is rotationally supported, a spheroidal stellar bulge, all surrounded by a massive dark-matter halo. In the following subsection we will describe the parameter choices for our fiducial model, which is designed to approximate a large, gas-rich Sbc disk galaxy. In § 5.2.1 we will also build an exact replica of the model used by S00, which will aid in our comparison; however, we postpone discussion of this model until then.

The initial disk is rotationally supported and is assumed to have the following distribution

$$\rho_d(R, z) = \frac{M_d}{4\pi z_0 R_d^2} \text{sech}^2\left(\frac{z}{2z_0}\right) \exp\left(-\frac{R}{R_d}\right), \quad (14)$$

where M_d is the disk mass, R_d is the radial disk scale length, and z_0 is the vertical scale height. The disk is in general composed of both gas and stars, with a gas mass fraction

$$f_d = \frac{M_{d,\text{gas}}}{M_d}. \quad (15)$$

We also allow for the possibility that the gas and stellar disks may have different radial distributions. While we continue to assume that both distributions follow Equation (14), we will set the gas radial disk scale length $R_{d,\text{gas}} = \alpha R_d$.

We also define m_d and m_g , the stellar and gaseous disk mass fractions, as

$$m_d = \frac{M_{d,\text{stars}}}{M_{\text{vir}}} \quad (16)$$

and

$$m_g = \frac{M_{d,\text{gas}}}{M_{\text{vir}}}, \quad (17)$$

where M_{vir} is the total virial mass of the galaxy, including all components, and $M_d = M_{d,\text{stars}} + M_{d,\text{gas}}$.

The vertical structure of the stellar disk is fixed by requiring that the disk be Toomre stable, i.e., $Q \geq 1$. In practice, this results in a z_0 that is set to 20% of the radial disk scale length R_d , and a vertical velocity dispersion of $\sim 40 \text{ km s}^{-1}$ at R_d , both consistent with observations (see e.g., Bottema 1993).

The vertical structure of the gaseous disk is more complicated as the temperature is fixed by the equation of state, rather than the velocity dispersion (which is, in turn, fixed by our choice of z_0). This formalism has recently been updated by Springel et al. (2005b) to account for pressure gradients in the gas disk and hence, they claim, can be used to construct purely gas disks. While we have not thoroughly investigated the effects of their new method, nor are we using it here, we note that after an initial equilibration period our disk, with a relatively high gas fraction, is quite stable. This will be shown in the following section.

We also allow for the inclusion of a centrally concentrated stellar bulge. The bulge, when included, is non-rotating and has a spherically symmetric exponential distribution

$$\rho_b(r) = \frac{M_b}{8\pi R_b^3} \exp\left(-\frac{r}{R_b}\right). \quad (18)$$

The exponential distribution is supported by observations which show that late-type spirals typically have bulge profiles more consistent with exponential than the commonly assumed $r^{1/4}$ profile (de Jong 1996; Balcells et al. 2003). In order to allow for this second possibility, we also allow our model bulges to follow the Hernquist (1990) distribution

$$\rho_b(r) = \frac{M_b}{2\pi} \frac{a}{r(r+a)^3}. \quad (19)$$

We found very little difference in the star formation between the two bulge distributions, and thus all galaxies in this work contain a bulge described by Equation (18).

The disk-bulge system is surrounded by a massive dark-matter halo. The dark matter profile is assumed to follow the Navarro-Frenk-White (NFW) fitting formula (Navarro, Frenk & White 1997), characterized by two quantities, M_{vir} , the total mass, and the halo concentration R_{vir}/r_s , where R_{vir} is the virial radius and r_s is a scale radius. In all of the galaxy models studied in this paper, the dark halo is contracted due to the adiabatic growth of the central baryons (Blumenthal et al. 1984; Flores et al. 1993; Mo et al. 1998; Gnedin et al. 2004).

The angular momentum of the dark halo is set by the spin parameter λ . In the Mo et al. (1998) model for disk formation, the specific angular momentum of the baryonic component is conserved, and thus fixing j_d , the disk angular momentum fraction, sets the size of the corresponding disk. We keep this formalism for the stellar disk, but treat the

gaseous disk separately. The gas disk, whose size is a specific fraction (α) of the stellar disk, has a much larger angular momentum fraction, j_g .

Once the above parameters are selected, the compound galaxy is constructed in a manner suggested by Hernquist (1993a), Springel & White (1999), and S00. In short, this method fixes the mass distribution according to the above formula, and then assumes the velocities can be approximated by the Jeans equations. We refer the interested reader to these works for more details.

Each disk galaxy is represented by N particles. In §5.1 we investigate the choice of N by running some higher resolution simulations. Motivated by the criteria of Power et al. (2003), all simulations presented here adopt a gravitational softening length $h = 400$ pc for the dark matter particles and 100 pc for the stellar and gas particles. We remind the reader that, in GADGET, forces between neighboring particles become non-Newtonian for separations $< 2.3 h$.

Now that we have outlined the basic ingredients of our disk galaxy model, we next introduce the specific model used for our investigation of star formation and feedback.

3.1.1 Sbc Galaxy Model

Since our primary goal in this work is to investigate star formation and feedback parameters, we select a galaxy model which is gas-rich and thus likely to be gravitationally unstable. To this end we choose a large gas-rich disk galaxy whose properties are motivated by local Sbc galaxies. This type of initial condition has the added benefit that the large gas supply provides a significant fuel supply and is thus likely to generate a large burst of star formation when participation in a galaxy merger. Furthermore, large, gas-rich disks such as this may be similar to disks at high redshift where gas fractions are presumably higher.

Because we choose the parameters of this model from observations of local Sbc's, we will need to make some inferences to translate the observed quantities to our model inputs. To begin, we note that the optical radius R_{opt} , dynamical mass M_{dyn} , ratio of HI to M_{dyn} within the optical radius, and absolute blue luminosity L_B are neatly compiled as a function of Hubble type in Roberts & Haynes (1994). Thus, for instance, the radial disk scale length is determined from the optical radius by assuming the relation $R_{\text{opt}} = 3.2 \times R_d$, which is valid for a Freeman disk.

Next, the bulge-to-disk ratio and bulge size are constrained to be consistent with the Sbc galaxies as found in de Jong (1996). Because we have selected a late-type spiral, this necessarily results in a small compact bulge. We can determine the total stellar mass by using the average Sbc B-band luminosity L_B and the B-band mass-to-light ratio of 1.0 found for late-type spirals (Bell & de Jong 2001). The total stellar mass and the bulge-to-disk ratio can be used to determine the exact mass in both the stellar disk and bulge components. We note that with these assumptions the bulge makes up slightly less than 10% of the baryonic mass.

Sbc galaxies are gas-rich. Observationally, there is a wide range of gas properties associated with Sbc galaxies, but in general, the gas component is roughly exponentially distributed and more extended than the stellar disk (Broeils & van Woerden 1994). Taking this into consideration, we assume the gas disk to have an exponential profile

with a gas scale radius R_g which is a factor α times the stellar disk scale radius, R_d . Based on the most extended distribution for Sbc galaxies reported in Broeils & van Woerden (1994), we choose $\alpha = 3$. The mass of the gaseous components can be found from the ratio of HI to M_{dyn} within the optical radius, with our assumed profiles, corrected for helium.

At this point, the mass and distribution of the baryonic components are completely specified. However, the dark matter distribution is not. In order to get some handle on the dark mass and profile we can use the dynamical mass. In practice, we assume an adiabatically contracted NFW halo with a concentration of 11 and then iteratively search for dark matter mass which gives us the correct dynamical mass at R_{opt} . This procedure results in a dark halo which is $8.1 \times 10^{11} M_{\odot}$. The resulting rotation curve has a maximum speed of approximately 204 km s^{-1} which is larger than the $\sim 190 \text{ km s}^{-1}$ suggested by the baryonic Tully-Fisher relation (Bell & de Jong 2001). The large rotation velocity of this model is a typical byproduct of adiabatically contracting an NFW halo (see, e.g., Cole et al. 2000).

The above procedure does not use the halo spin parameter to set the size of the stellar disk. Arguably, the actual scale lengths of galaxies are more well constrained than halo spin parameters. This also means that the angular momentum of the disk components is independent of the halo angular momentum. The halo spin parameter was set to the median value from Bullock et al. (2001). Decoupling of the halo and disk angular momenta is also motivated by the discrepancy between the specific angular momentum distribution of a typical dark matter halo and that of an exponential disk (Bullock et al. 2001).

Each disk galaxy is represented by 170,000 N-body particles, 100,000 of which represent the dark-matter halo, 30,000 each for the stellar and gas disks, and 10,000 for the bulge. In §5.1 we investigate our choice of particle number. Table 2 lists the properties for our Sbc disk-galaxy model.

3.2 Star Formation

The feedback model outlined in §2 was designed to stabilize the gas disk and prevent excessive star formation due to instabilities in the gas disk. To test our model, the Sbc galaxy model was simulated in isolation for one Gyr, with the last nine parameter sets in Table 1. The resulting star-formation rates are shown in Fig. 1. Except for *n0low* and *n1low*, all models have continuous star formation at a roughly constant rate. The spikes of large star formation in the first ~ 100 Myr of the simulation result from the initial model not being exactly in equilibrium. In particular, the feedback reservoir q is empty at the beginning of the simulation and thus provides no pressure support in the initial disk. The low-feedback parameter sets have star-formation rates of over $10 M_{\odot} \text{ yr}^{-1}$, the medium-feedback parameter sets $2 - 3 M_{\odot} \text{ yr}^{-1}$, and the high-feedback parameter sets $< 1 M_{\odot} \text{ yr}^{-1}$. The equation of state index, n , has a relatively minor effect on the average star-formation rate of the isolated galaxies. For instance, run *n0med* has an average star-formation rate of $3.3 M_{\odot} \text{ yr}^{-1}$, while the average of *n2med* is $3.0 M_{\odot} \text{ yr}^{-1}$.

Figure 2 displays the gas surface density for the models. All models with constant star formation are qualitatively similar. In the *n0low* and *n1low* models, the gas disk

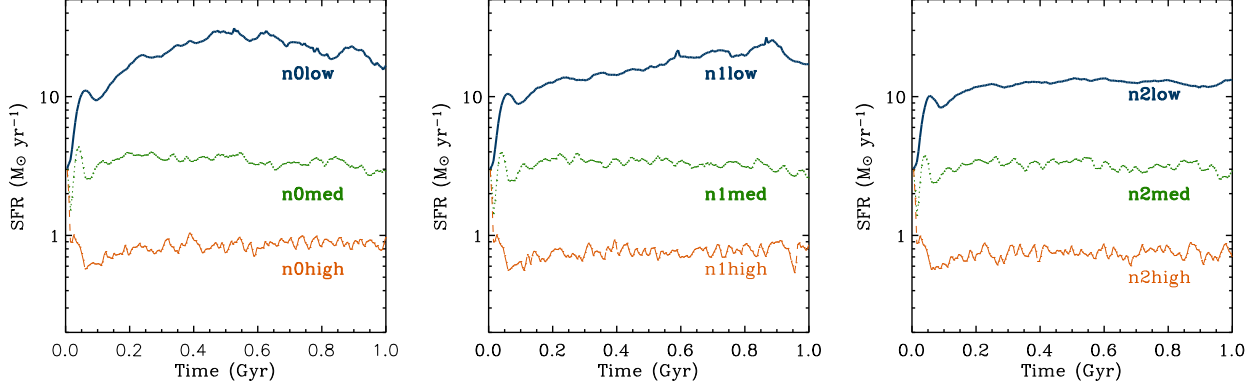


Figure 1. Star formation for an isolated Sbc disk galaxy. The left, middle and right show the runs for the $n = 0, 1$ and 2 , feedback models, respectively. The “low” feedback model has the highest star-formation rate and the “high” feedback model has the lowest rate. For a given n , the star-formation rate scales roughly as $\tau_{\text{fb}}^{-1/2}$.

has fragmented due to the growth of instabilities in the inner disk. The $n2low$ model also looks fragmented, but its star formation rate is still regulated at a constant rate of $10 \text{ M}_{\odot} \text{ yr}^{-1}$. This evolution is consistent with other studies that have evolved isolated disks with insufficient feedback (S00; Bottema 2003; Robertson et al. 2004; Springel et al. 2005b; Li et al. 2005, 2006). We also note that these instabilities were likely seeded by noise in the potential (Toomre 1981; Hernquist 1993a) and because the initial disk is not in perfect equilibrium. In the stable disks, this noise is then swing amplified to produce a spiral pattern. Representing the halo with a fixed potential or increasing the number of particles used for the halo both delayed the onset of gravitational instabilities or spiral structure.

The gravitational instabilities are also manifested in the star-formation rates which are much larger than the stable disks’ and are not maintained at a constant value. This is especially apparent in the $n0low$ and $n1low$ models in which run-away star formation progresses until a large fraction ($\sim 60\%$) of the original gas is consumed. In general, however, relatively little of the original gas is converted to stars during the 1 Gyr evolution we follow; only $\sim 5\%$ for the *high* feedback models and $\sim 20\%$ for the *medium* feedback models. One reason for these low gas consumptions is the very extended distribution of gas. Half of the original gas mass is at radii greater than 27.6 kpc, whereas star formation predominantly takes place at the galaxy center and along transient spiral structures, always at radii less than 25 kpc. A more subtle feature is the transient spike of star formation at $T \approx 0.05$ Gyr, present in all models, that results because the initial system is not in perfect equilibrium. One reason for this is that the initial feedback reservoir is initially empty and requires a small amount of star formation to fill it sufficiently enough to provide pressure support. We tested one simulation that started with a filled feedback reservoir and while the initial transient star-formation rate was suppressed, the evolution beyond $T = 0.1$ Gyr was unchanged.

Within our model, the time-averaged star-formation rate in a quiescent spiral disk is directly set by τ_{fb} . Figure 1 demonstrates that each *low*, *med*, and *high* feedback model forms stars at a nearly constant rate, regardless of n . We can understand the origin of this scaling by considering that

the gas disk is in hydrostatic equilibrium within the galaxy potential. Since the gas is a small fraction of the total mass, the potential and thus the gas pressure (if it is in hydrostatic equilibrium) are expected to be fixed by the galaxy model. In other words, the gas pressure is constant regardless of the specific feedback model. For star-forming gas, where the effective pressure is provided by Equation (11), this yields a simple relation between the gas density and the feedback timescale

$$\rho \propto \tau_{\text{fb}}^{-1/(1+n/2)}. \quad (20)$$

Since the integrated star formation rate is

$$SFR \propto \dot{\rho}_* V \propto \dot{\rho}_* / \rho \propto \rho^{0.5}, \quad (21)$$

where the third proportionality comes from Equation (1), it follows that

$$SFR \propto \tau_{\text{fb}}^{-1/(2+n)}. \quad (22)$$

In the simplest, $n = 0$, case the star-forming gas has an isothermal equation of state and Equation (22) predicts the star formation to scale as $SFR \propto \tau_{\text{fb}}^{-1/2}$. In our range of models, τ_{fb} was varied by factors of ten so that we expect the star formation rates to vary by a factor of $\sqrt{10} \sim 3$. This appears to match the simulated star-formation rates quite well, where the values for the *high*, *med*, and *low* models are $\sim 1, 3$, and 10 .

These star-formation scalings are complicated by the distinct density threshold for star formation as well as the self-gravity of the gas. In particular, the $n = 2$ model appears to follow the $\tau_{\text{fb}}^{-1/2}$ scaling the closest, yet its expected scaling is a much softer $\tau_{\text{fb}}^{-1/4}$. The reason for this discrepancy, as we will see more clearly in § 3.5, is that most of the gas within these models piles up at the threshold density for star formation ρ_{th} and thus has the effective temperature at this density (T_{eff} in Table 1). Thus, the gas scales as an isothermal gas rather than $n = 2$.

3.3 The Kennicutt Law

Star formation in the simulations was designed to be consistent with the empirical Kennicutt law (Kennicutt 1998,

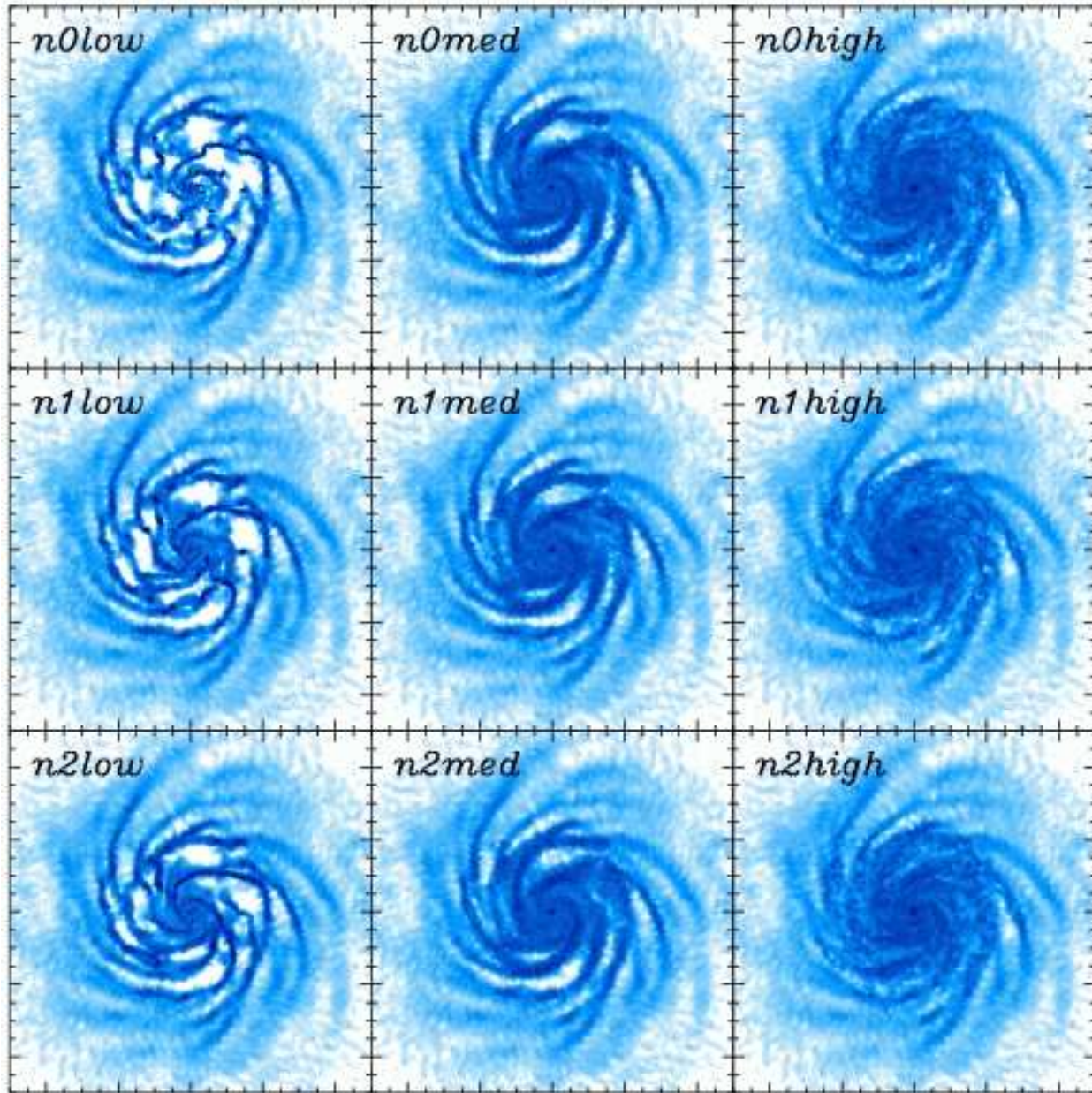


Figure 2. Projected gas density for the Sbc disk galaxy model for each parameter set shown after 500 Myr, or ~ 3 rotation periods at the half-mass radius, of evolution. The “low” parameter sets have led to the break up of the gaseous disk and hence accelerated star formation as shown in Fig. 1.

Equation 2). The success of this is verified in Figure 3, where we show the star-formation rate and gas mass averaged in azimuthal annuli for the isolated Sbc galaxy simulations. The Kennicutt law is shown as a straight black line, which the simulations closely track.

While Figure 3 demonstrates that all simulated disks track the Kennicutt law at high gas surface densities, the simulations that included a threshold density ρ_{th} fall below the Kennicutt law at lower gas surface densities. As mentioned previously, a similar feature is observed by Kennicutt (1998) near $\sim 10 \text{ kpc pc}^{-2}$. Figure 3 also shows that higher feedback models fall below the Kennicutt law at higher gas surface densities. This is a result of the increased vertical scale height owing to the high feedback pressurization.

To ensure that it is ρ_{th} that sets the departure from the observed Kennicutt law we reran the three medium feedback models (*n0med*, *n1med*, and *n2med*) with $\rho_{\text{th}} = 0$. Figure 3 shows that these simulations closely track the Kennicutt law across all gas densities.

3.4 Disk Scale Heights

The differences in star-formation rates between the low-, medium-, and high-feedback parameter sets is accompanied by corresponding differences in the scale height of the gas. The medium-feedback simulations have scale heights of ~ 300 parsec at a radius of 5 kpc, increasing to 450 parsec at 25 kpc where star formation ceases. The high-feedback simu-

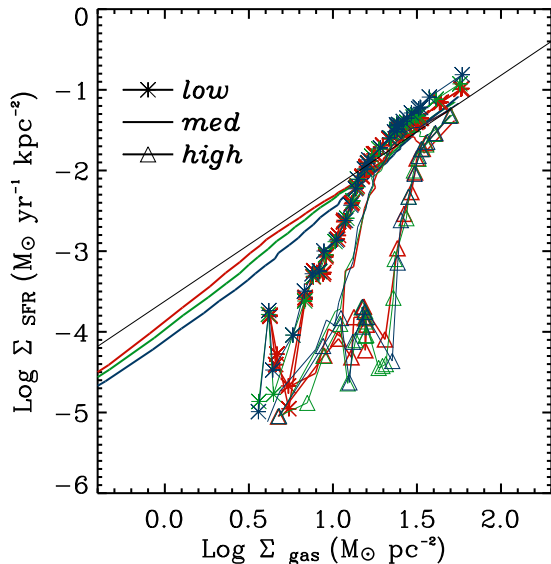


Figure 3. Star-formation rate per unit area and gas surface density averaged within azimuthal annuli for the fiducial isolated Sbc disk galaxy at $T = 0.1$ Gyr. Shown with different symbols are the *low* (asterisks), *med* (continuous line), and *high* (open triangles) parameter sets for each value of n ($0 = \text{blue}$, $1 = \text{green}$, $2 = \text{red}$). Also shown are three *med* feedback runs that did not include an explicit gas density threshold for star formation. The straight (black) line is the empirical Kennicutt law. This plot can be directly compared to Figure 3 from Kennicutt (1998).

lations, in contrast, have scale heights of 450 parsec at 5 kpc radius, increasing to 500 parsec at 25 kpc. The $n = 0$ and 1 low-feedback simulations do not have a well defined scale height because the unstable disk has fragmented. The $n = 2$ low-feedback simulation has a scale height of ~ 200 parsec, near the numerical resolution of our simulations.

For a given value of τ_{fb} , the vertical structure is independent of the value of n . This fact, which may be surprising at first, arises because for all these models the feedback is efficient enough to limit the maximum gas density to slightly above the threshold density while most of the gas is at densities slightly below the threshold, even in the star-forming regions of the disk. Since n describes the scaling of effective pressure with density above the threshold, and the star-forming gas is confined to a narrow range of densities above the threshold, it follows that n has only a very small influence on the structure of the isolated galaxies. (As mentioned earlier, for gas below the threshold density a value of $n = 2$ is used in all cases.)

The fact that the star formation comes from gas at the threshold density also explains how a $\sim 50\%$ difference in scale heights between the med- and high-feedback sets can explain a difference in star formation rate of more than a factor of 3. Without a density threshold, Equation (1) predicts that the integrated star-formation rate should scale as $\rho^{1/2}$, but at the threshold density the effective star-formation law is much steeper than indicated by Equation (1).

3.5 Phase Diagram

To illustrate the effects of our pressurizing feedback, and its dependence on the free parameters τ_{fb} and n , we present temperature–gas density phase diagrams in Figure 4. On the vertical axis of the phase diagram is the effective temperature, which includes a contribution, if any, from the feedback reservoir. There are several lines plotted in Figure 4 that delineate distinct phases of gas. The horizontal line at 10^4 K shows the initial gas temperature as well as the minimum of the cooling function. Most low-density gas resides near this temperature.

The feedback reservoir becomes significant for gas which is above the threshold density for star formation ρ_{th} , shown by the vertical solid line in Figure 4. At high gas densities ($\rho_{\text{gas}} \geq \rho_{\text{th}}$) star formation acts to maintain the gas at a temperature and pressure specified by Equations (10) and (11), which is shown by a dotted line in Figure 4. From these relations it is apparent that the slope of the dotted line is specified by n , and the normalization by the combination $c_* \tau_{\text{fb}}$. For example, when $n = 0$, star-forming gas is isothermal with an effective temperature of 2.5×10^4 K, 2.5×10^5 K, and 2.5×10^6 K (see Table 1) for the *low*, *med*, and *high* models, respectively.

Figure 4 demonstrates the effects of the equation of state in star-forming regions set by n . For instance, the *n0low* model is nearly identical to no feedback at all. Gas is always close to 10^4 K, and the disk is insufficiently pressurized and subsequently fragments (see Figure 2). In the case of *n2low*, however, the steep equation of state above ρ_{th} means that high-density gas eventually becomes pressurized and limits the amount of fragmentation.

In general, the gas phases below the threshold density ρ_{th} are very similar for each *high*, *med*, and *low* model, regardless of n . For the medium- and high-feedback models, the high temperature and significant pressurization cause a large amount of the gas to pile up at ρ_{th} . This effect is a byproduct of the long timescale for energy dissipation, set by τ_{fb} , in the *high* and *med* models. In this scenario, because of recent star-formation, the feedback reservoir has been filled and the increased pressure support has pushed the particles to densities below ρ_{th} .

For the quiescent spiral galaxy we simulate here, we have not included any diffuse hot gaseous halo. Thus, gas only becomes hot ($> 10^4$ K) because of star formation. We also expect hot diffuse gas to be efficiently produced by shocks (Cox et al. 2004) and active galactic nuclei (Cox et al. 2006) that may attend the galaxy merger. This will be explicitly shown in § 4.3.

4 MAJOR MERGERS

To generate a galaxy merger, identical copies of the isolated galaxy model are initialized on a prograde parabolic orbit with pericentric distance $R_{\text{peri}} = 11$ kpc ($\sim 2 R_d$ or $\sim 0.05 R_{\text{vir}}$) and an initial separation of 200 kpc. One disk is in the orbital plane while the other is inclined by 30° . This generates a fast, nearly radial, collision consistent with orbits found for dark-matter halos in a cosmological simulation (Khojfar & Burkert 2006).

Figure 5 displays the stellar (disk plus bulge) density

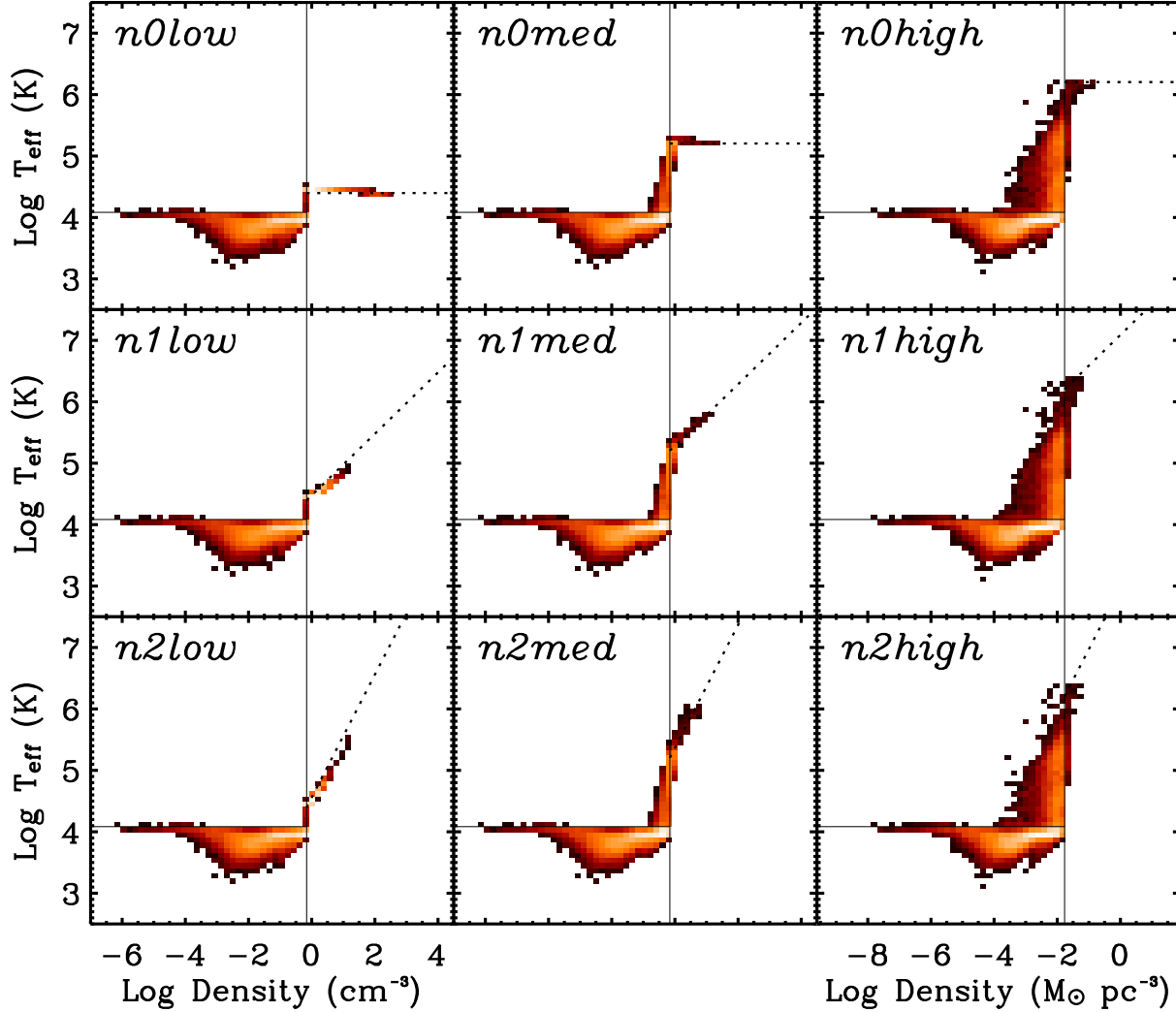


Figure 4. Each panel shows the effective temperature – gas density phase diagram for the isolated Sbc disk at $T = 0.25$ Gyr for the entire set of feedback models considered. The effective temperature is calculated as $T_{\text{eff}} = \bar{\mu} P_{\text{eff}} / k\rho$, where P_{eff} is given by Equation (5). The vertical line shows the threshold gas density for star formation ρ_{th} , and the horizontal line at 1.2×10^4 K is a guide to the eye that demarcates the floor of the cooling function. The expected effective temperature determined by our feedback model, Equation (10), is shown by a dotted line at densities above ρ_{th} .

projected onto the orbital plane and Figure 6 shows the projected gas density from an equivalent viewing angle. The simulation begins with a wide separation between the two galaxies, and they are essentially unaffected by each other's presence.

As the galaxies reach pericenter ($T \approx 0.6$ Gyr) each disk becomes tidally distorted. Long tidal tails carry out loosely bound material while the central regions form transient bar-like structures (see $T = 0.7$ – 0.9 Gyr). At this point dynamical friction has increased the spin of the dark-matter halos and extracted orbital energy from the originally unbound orbit. As the galaxies separate, a bridge forms that connects the two galactic centers, and at $T = 1.1$ Gyr the galaxies reach apocenter, with a separation of 80 kpc.

The final merger is a messy process starting at $T = 1.6$ Gyr and lasting for 200 Myr. The disks are effectively destroyed and we are left with a spheroidal-looking ob-

ject (MH96; S00; Hernquist 1992). Owing to gas shocking, kinetic energy is converted to thermal energy and subsequently radiated away. This results in an offset between the stellar and gaseous components that torques the gas into the dense central regions of each galaxy (see $T = 0.7$ – 0.9 Gyr). Since we have tied the formation of stars to the gas density through Equation (1), a burst of star formation ensues (MH96; Mihos & Hernquist 1994c). From $T = 1.2$ – 1.6 Gyr, the extended distribution of the gaseous component produces long tidal tails while the stellar tails have already fallen back to the central galaxy. These gaseous tails are sharper and thinner than their stellar companions, and continually rain back on the central disks.

The final merger is particularly violent for the collisional gas as large amounts of gas shocking occur (Cox et al. 2004). These shocks provide a significant source of heating to the gas, and its evolution depends on its density. High-density

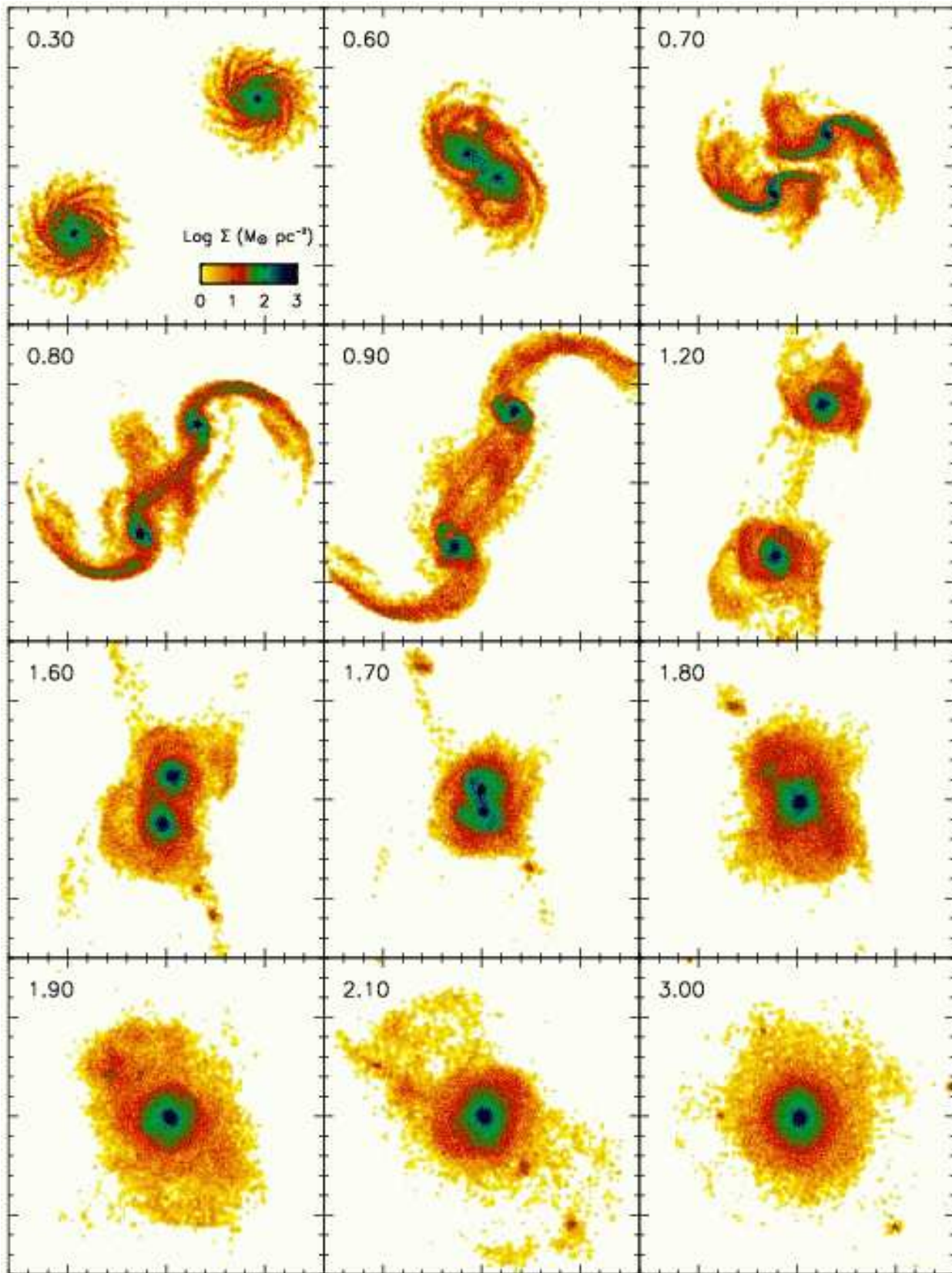


Figure 5. Projected stellar (disk plus bulge) density during the *n2med* major merger. Each panel measures 160 kpc on a side, and the number in the upper left of each frame is the simulation time measured in Gyr. The disk galaxy initially on the lower left is coplanar with the orbital plane while the upper right disk is tilted by 30° . The logarithmic density scale, in units of $M_\odot \text{pc}^{-2}$, is given by a colorbar in the upper-left plot.

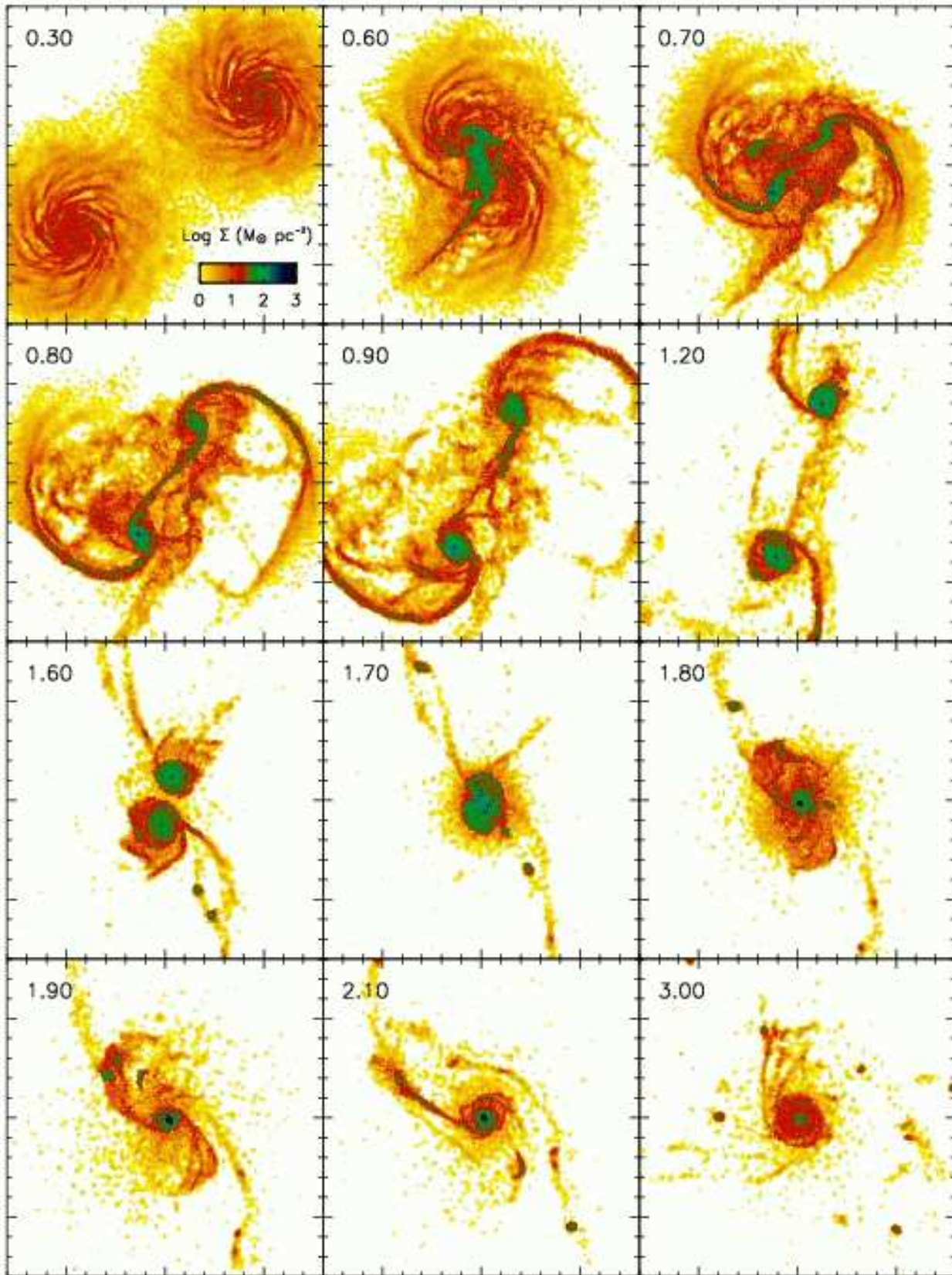


Figure 6. Same as Fig. 5, except here the projected gas density is shown. The density scale is identical to Fig. 5 and is given in the top-left plot.

gas is able to radiatively cool on a short time-scale, and provides fuel to continue the starburst. Low-density gas, on the other hand, expands from the central region and contributes to a hot gaseous halo in the merger remnant. At $T = 3.0$ Gyr, 1.2 Gyr after the merger is complete, $\sim 18\%$ of the current gas content has cooled and has formed a nuclear (< 10 kpc) disk, similar to what was found by Barnes (2002) and Springel & Hernquist (2005). The merger remnant also contains several tidal condensations, formed from loosely bound tidal material and composed entirely of gas and new stars (c.f., Barnes & Hernquist 1996; Duc et al. 2004).

4.1 Star Formation

Figure 7 displays the star-formation rate during the simulated major merger for all feedback parameter sets. The star-formation history is punctuated by several significant dynamical events. Prior to the first close passage ($t < 0.5$) the star-formation rate is that of two quiescent disks. The first encounter of the disks, at $T = 0.58$ Gyr, produces a strong shock between the gas disks and a ridge of high density gas stretches across both disks. This feature generates an enhancement of the global star-formation rate, especially in the low and medium feedback models.

Subsequent to the first passage, starting at $T \sim 0.65$ Gyr, tidally ejected gas is steadily stripped of its angular momentum and continuously falls back on the original disk galaxy. This process lasts for ~ 1 Gyr, but the resulting star-formation rate is strongly influenced by the feedback model. The low-feedback models provide gas with minimal pressure support. Gas quickly reaches high densities in the galaxy center, fueling a prolonged burst of star formation. High-feedback models provide much stronger pressure support, which limits the amount of gas at high density and hence the star-formation rate.

At first glance, the prolonged star formation during and immediately after the first disk encounter seems at odds with the results of MH96 and S00, whose progenitor disks, which contained a bulge as ours do here, demonstrated very minor star formation after the first encounter. In fact, the galaxy models employed by MH96 and S00 contained bulges more massive (one-third the disk mass) than that used here (one-tenth the disk mass), and a much smaller fraction of gas. As noted by MH96, this suggests that the suppression of gaseous inflow due to the presence of a bulge is very dependent upon the bulge mass and the disk composition. More work will be needed to quantify the relationship between bulge mass, galaxy composition, and early gas inflow leading to bursts of star formation.

The final merger is preceded by an increase in the star formation rate at $T \sim 1.6$ Gyr. At this time, gas begins to see the nuclei as a single potential, while it is also being stripped of angular momentum due to the abundant shocks that occur. At $T = 1.8$ Gyr, the final coalescence occurs. The strongest burst of star formation precedes the merger by ~ 50 Myr in every model. The strength and duration of this burst is a strong function of the feedback model. Models with isothermal equations of state have a strong, prolonged burst (except the *n0low* and *n1low* models, which by this time have consumed a large portion of the available gas), while the models with stiffer equations of state suppress

Table 3. Star formation properties of major merger simulations. Here e is the fraction of the original gas consumed by star formation during the entire 3 Gyr simulation. SFR_{max} is the maximum star formation rate during the merger. T_{LIRG} is the duration, in Gyr, at which the star formation rate is greater than $20 M_{\odot} \text{yr}^{-1}$, corresponding to when this galaxy pair would be classed as a luminous infrared galaxy, LIRG.

Model	e	SFR_{max} ($M_{\odot} \text{yr}^{-1}$)	T_{LIRG} (Gyr)
<i>n0low</i>	0.70	78	1.55
<i>n0med</i>	0.55	159	1.31
<i>n0high</i>	0.25	51	0.25
<i>n1low</i>	0.69	84	1.72
<i>n1med</i>	0.51	105	1.29
<i>n1high</i>	0.24	43	0.08
<i>n2low</i>	0.67	75	1.85
<i>n2med</i>	0.47	56	1.34
<i>n2high</i>	0.18	44	0.04

large bursts of star formation due to the efficient pressure support provided by the feedback reservoir.

To provide a more quantitative view of the star formation induced by the galaxy merger, we calculate the fraction e of the original gas converted to stars during the simulation. Table 3 lists e for each merger. Two trends are noticeable for e , both consistent with the isolated disk galaxy simulations: first, high-feedback models consume less than half as much of the original gas as the low-feedback models do, for equivalent n . Second, models with a stiffer equation of state (i.e., higher n) suppress gas consumption, although this is a much smaller effect.

Another relevant measure of the global star formation is the peak star-formation rate SFR_{max} , which is also listed in Table 3. The equation of state n has a much larger influence on SFR_{max} than on e . For example *n0med* has a SFR_{max} roughly three times larger than *n2med*, yet the overall gas consumption is larger by only 8%. Similarly, the peak star-formation rate of *n2high* is only 20% lower than *n2med*, while the gas consumption is less than half as much.

The different dependence of e and SFR_{max} on the feedback parameters results from the varying effects of τ_{fb} and n . The effective pressure is proportional to τ_{fb} (see Equation 11), thus large values produce significant pressure support and restrict the amount of gas that can reach star-forming densities. Thus the overall gas consumption e is primarily a result the value of τ_{fb} . On the other hand, once gas reaches star-forming densities, n determines the ability of this gas to reach even higher densities, and because the star-formation rate scales non-linearly with density (see Equation 1) the maximum star-formation rate SFR_{max} is a strong function of n .

It is interesting to note that the simple star-formation rate scaling, derived as a function of τ_{fb} in Equation (22), that only moderately described the behaviour of the isolated galaxies, performs much better for the merging galaxies star-formation rates. Recall that the expected scaling was $\text{SFR} \propto \tau_{\text{fb}}^{-1/(2+n)}$. Applying this to the maximum star-formation rate, we would expect a ratio of 3.2, 2.2, and 1.8 for the $n = 0, 1,$ and $2,$ respectively. The ratios between the

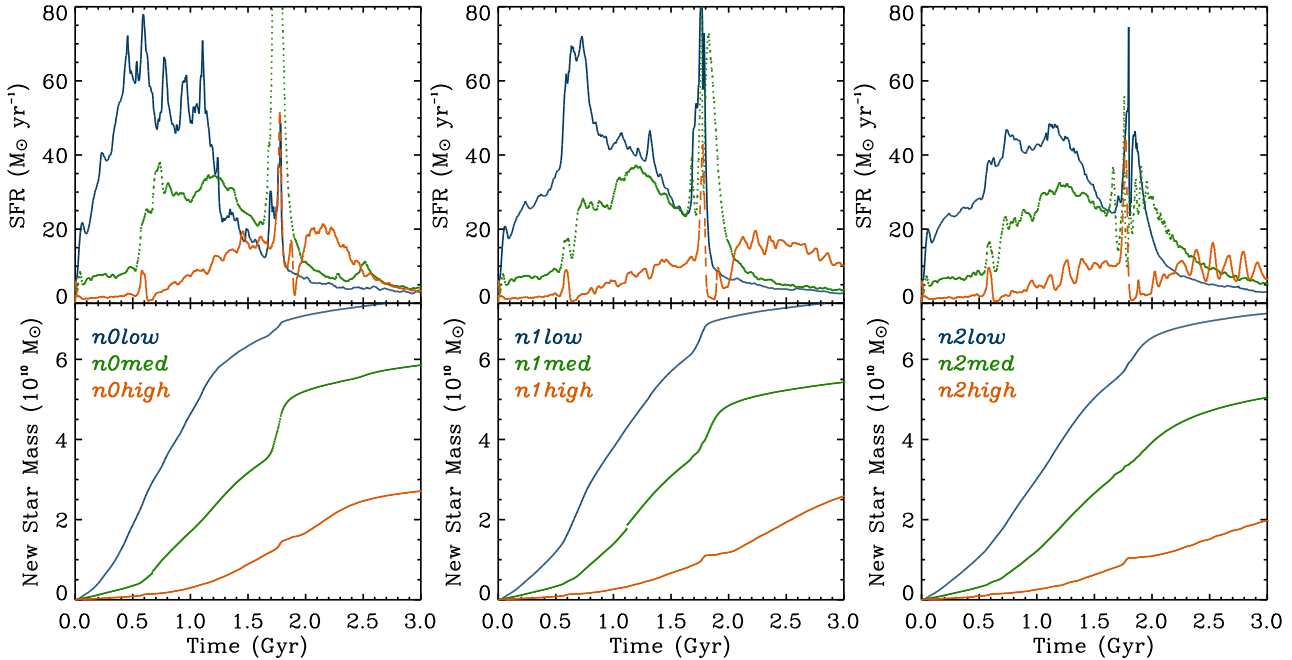


Figure 7. Star formation for a major merger between two identical Sbc disk galaxies. The $n = 0, 1$, and 2 feedback models are shown in the top, middle and bottom panels, respectively. In every instance the low feedback model has a higher star-formation rate than the high feedback model between $T \lesssim 2$ Gyr. The final merger occurs at $T = 1.8$ Gyr and this is coincident with the highest peak of star formation in all models with sufficient feedback to stabilize the isolated disks, i.e. the medium- and high-feedback parameter sets.

med and *high* runs from Table 3 are 3.1, 2.4, and 1.3. Because of the unregulated star formation in the *low* models, the scaling appears to break down for these.

One interest in studying star formation induced by galaxy mergers is their possible relation to luminous infrared galaxies (LIRGs; Sanders & Mirabel 1996). LIRGs are classified as galaxies which have an infrared luminosity greater than $10^{11} L_{\odot}$ and hence are forming stars at $\geq 20 M_{\odot} \text{ yr}^{-1}$ (using the L_{IR} -SFR conversion of Kennicutt 1998). Listed in Table 3 is T_{LIRG} , the total time during the merger in which this system would be detectable as a LIRG. The choice of feedback has a significant effect on the length of time this merger would classify as a LIRG. We note that we have not distinguished between the two progenitors, and thus do not account for viewing angles where the two galaxies would be classified as separate. Nor have we included a full treatment of the obscuring effects of dust and its re-radiation in the infrared (but see Jonsson 2004; Jonsson et al. 2006; Jonsson 2006).

It is clear that these three quantities do not describe the full star-formation history of each model. Instead, they are gross measures, useful to characterize the effects n and τ_{fb} have on the star formation induced by a galaxy major merger. Future work will compile quantities such as these for a wide range of initial conditions, assumed merger orbits, and merger mass ratios. These relations will be useful in analytic or semi-analytic models of galaxy formation, and in using observations to clarify which feedback models are realistic.

As a final remark related to the star-forming histories shown in Figure 7, we draw attention to the oscillatory star formation that occurs in nearly every model, but is most pronounced in the high-feedback models. These oscillations

occur primarily after peaks in the star formation rate and are thus clearly visible after the first passage and the final burst. However, even the isolated disk high-feedback models contains some oscillatory star formation. The periods of oscillation are almost exactly $2 \times \tau_{\text{fb}}$, the thermalization timescale, indicating that the oscillations result from the interplay between pressurizing feedback efficiently quenching star formation followed by the dissipation of this pressure support, gravitational collapse, and an increase in the star-formation rate.

4.2 The Kennicutt Law

In § 3.3 we demonstrated the the individual spiral galaxies matched the empirical Kennicutt law (Kennicutt 1998, Equation 2), as they were designed to do. In Figure 8, we show the star-formation rate and gas mass averaged in a 2 kpc aperture plotted at representative times during each merger. As was done previously, we overplot the Kennicutt law with a solid black line, and the observed envelope for which *all* observations are contained is plotted with a dotted line. Similar to the isolated galaxies, the merger simulations closely track the empirical star-formation law. There are a few points that are above the upper envelope, however these are from the unstable *n0low* and *n1low* runs. The fact that all of the stable models agree with the Kennicutt law, regardless of n and τ_{fb} , suggests that it is our formulation of star formation according to Equation (1) and the value of the free parameter c_{\star} (which are identical for all runs) that determines the agreement with the Kennicutt law.

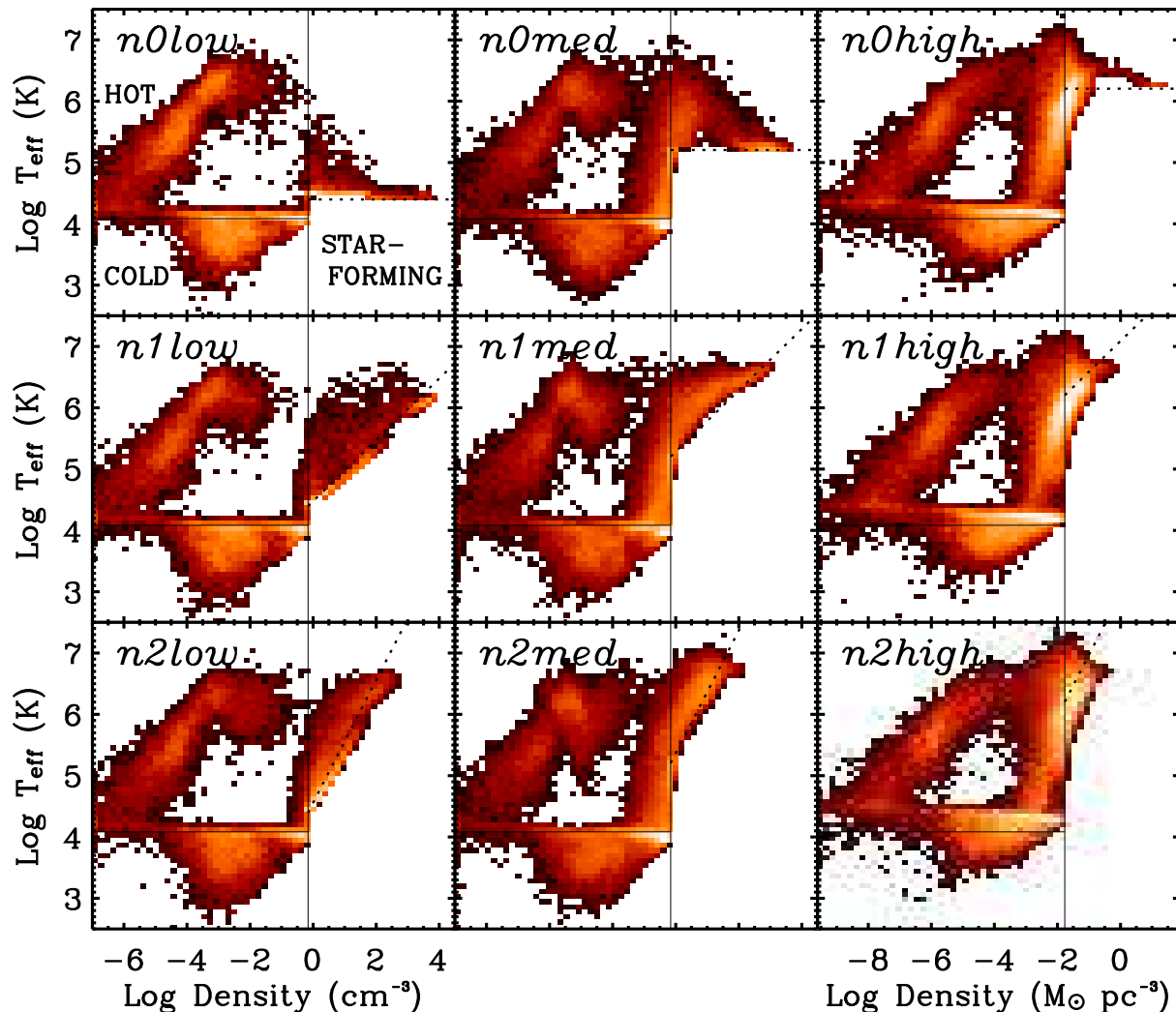


Figure 9. The effective phase diagram for the galaxy merger at $T = 1.75$ Gyr for all models. The calculation of T_{eff} and all of the lines are identical to Figure 4. The top-left panel (*n0low*) denotes the three phases of gas, hot, cold, and star-forming as described in the text.

4.3 Phase Diagram

At this point we revisit the phase diagrams originally introduced in § 3.5 in the context of isolated Sbc disk galaxies. We expect two differences when we look at the phase diagrams of the interacting galaxies in comparison to the isolated disks. First, the collisional shocks that attend the interaction generate a significant amount of hot low-density gas. Second, because of the interaction, much more gas will reach high densities.

Figure 9 shows the phase diagram for the galaxy merger of each parameter set at a point in time 50 Myr prior to the final coalescence. At this point, most models are near their peak of star-formation. All gas resides in one of three distinct regions in the phase diagram: hot, cold, or star-forming.

Gas which is below the critical density threshold for star formation ρ_{th} is designated as either in a hot or cold phase, depending on whether its temperature is above or below 1.2×10^4 K, denoted by a horizontal line in Figure 9. When the simulation begins, as well as in the isolated disks, all non-

star forming gas is cold owing to efficient cooling. This gas remains cold until the first passage, when gas contained in the tidal tails is ejected and adiabatically cools to $\sim 10^3$ K. Gas that is not part of the tidal material collides with gas from the other disk. These collisions generate shocks that heat the gas to temperatures well above 10^4 K where it is deemed hot. Because the cooling time of this hot, low-density gas is greater than the merger time-scale, most of this gas expands out of the central region and it remains in this phase until the merger is complete.

During the final merger, the significant collision results in shock heating, and therefore a lot of hot gas (Cox et al. 2004). While most of the gas remains hot after the final coalescence ($T \gtrsim 2.0$), some of the shock-heated gas cools and flows to the galaxy center. This gas, as well as the continual infall of tidal material, fuels the steadily decreasing star formation.

Gas which is at, or above, the threshold density for star formation is strongly affected by the feedback model. In this sense, the merger is similar to the isolated disk. The main

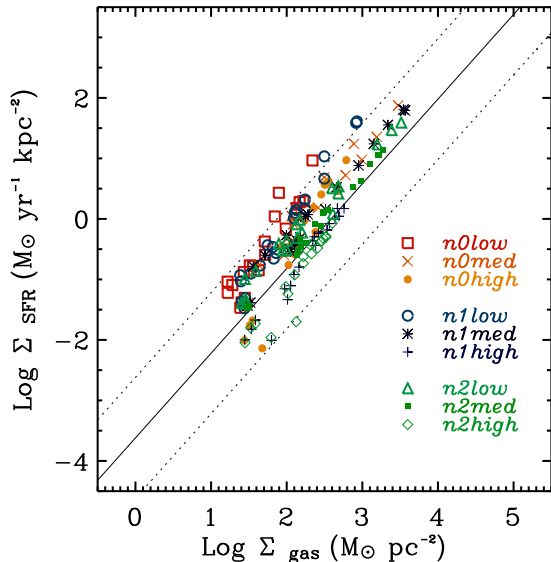


Figure 8. Star-formation rate per unit area and gas surface density averaged within an azimuthal aperture of radius 2.0 kpc, one point type for each simulation. For each run points are plotted every 200 Myr during the interaction, and every 50 Myr during the final merger. The solid line is the empirical Kennicutt law, and the dotted lines represent the envelope in which **all** observation reside. This plot can be directly compared to Figure 6 from Kennicutt (1998).

difference is that gas in the merger reaches much high densities than the in the isolated case. Figure 9 shows that, like the isolated disks, the effective temperature of star-forming gas is close to Equation (10), which is delineated with a dotted line in the figure.

Figure 9 also shows a large spread in the effective temperature of star-forming gas. This spread is considerably larger than in the isolated disks and is a direct result of the varied history of shock-heating, star formation, and feedback that attends the violent nature of the merger. Figure 9 also demonstrates that the med- and high-feedback models have a significant amount of gas that piles up at ρ_{th} owing to the pressure support provided by these models. This feature also relates to the oscillatory star formation discussed at the end of the previous section as gas continually cycles into and out of star-forming regions based upon their recent star-formation history, current dynamics, and dissipation of feedback reservoirs q .

4.4 Merger Remnants

Most of the merger simulations run to-date have focused on the role disk-galaxy major mergers may play in forming elliptical galaxies, as first suggested by Toomre & Toomre (1972) and Toomre (1977), and commonly referred to as the “merger hypothesis”. To this end, studies have addressed whether galaxy mergers can reproduce the $r^{1/4}$ surface brightness profile which many elliptical galaxies appear to have (Barnes 1992; Hernquist 1992, 1993c; Hernquist et al. 1993; Mihos & Hernquist 1994a; Barnes & Hernquist 1996; Springel 2000; Naab & Trujillo 2005), the kinematic

structure of merger remnants (Naab & Burkert 2003; González-García & van Albada 2005a,b; Cox et al. 2006), or if the merger remnants fall on the fundamental plane (Bekki & Shioya 1997; Bekki 1998; Naab & Burkert 2003; Dantas et al. 2003; Nipoti et al. 2003; Boylan-Kolchin et al. 2005, 2006; Robertson et al. 2006), a tight correlation between the velocity dispersion, effective radius, and luminosity, on which all ellipticals reside (Djorgovski & Davis 1987; Dressler et al. 1987; Bender et al. 1992; Bernardi et al. 2003; Padmanabhan et al. 2004). However, very few of these simulations have included recipes for star formation and feedback or explored how these parameters affect the remnant. In light of this, this section looks at the properties of the merger remnants to determine if studies of this sort might be sensitive to the prescriptions used to include star formation and feedback. We reserve a complete analysis of merger remnants for future work because this will require a much larger set of runs spanning a range of progenitor galaxy masses. Here, we simply present the stellar mass profile, the remnant size, as measured by R_e , the half-mass radius, and the one-dimensional central velocity dispersion for each merger remnant. We show that the size and velocity dispersion depend strongly on the feedback model while the stellar mass profile is only weakly dependent.

4.4.1 Stellar Mass Profiles

Figure 10 shows the azimuthally averaged surface density profile versus the fourth root of the projected radius for all merger simulations. A pure $r^{1/4}$ -type profile would be a straight line in this plot. Similar to the work of Mihos & Hernquist (1994a) and S00, the merger remnants show central cusps that are disjoint from the outer density profiles. The central-density excess begins at $R \sim 200$ pc, near our resolution limit, and is comprised of both stars that are newly formed during the merger (shown as a dotted line), as well as the pre-existing bulge. In higher resolution simulations (see §5.1) the profile changed very little, as indicated by the overplotted profile in the *n2med* panel, suggesting that it is not just poor resolution which generates the central profile cusp. Further, because all models shown in Figure 10 display a cuspy profile, it does not appear to be a result of the strength or density-dependence of the feedback model, although there is a trend for the high feedback models to form fewer stars and thus the surface density is predominantly bulge-dominated toward the center.

The ubiquitous nature of the central cusp indicates that it is a byproduct of our initial galaxy model. As noted by S00, the remnant has not forgotten about the dense stellar bulge in the progenitor disk. Even a collisionless run, shown as a dashed line in the lower-right plot, demonstrates a break in the surface density. We also performed one simulation without a central bulge which produced a profile that exhibited a more subtle upturn toward the center. Not surprisingly, the central density excess in this case was solely composed of stars formed during in the simulation. These results are consistent with Mihos & Hernquist (1994a) and S00.

It is not yet clear if the surface densities plotted in Figure 10 are consistent with observations, or even if there exists a definitive sample with which to compare these profiles. In a recent study of the K-band surface-brightness pro-

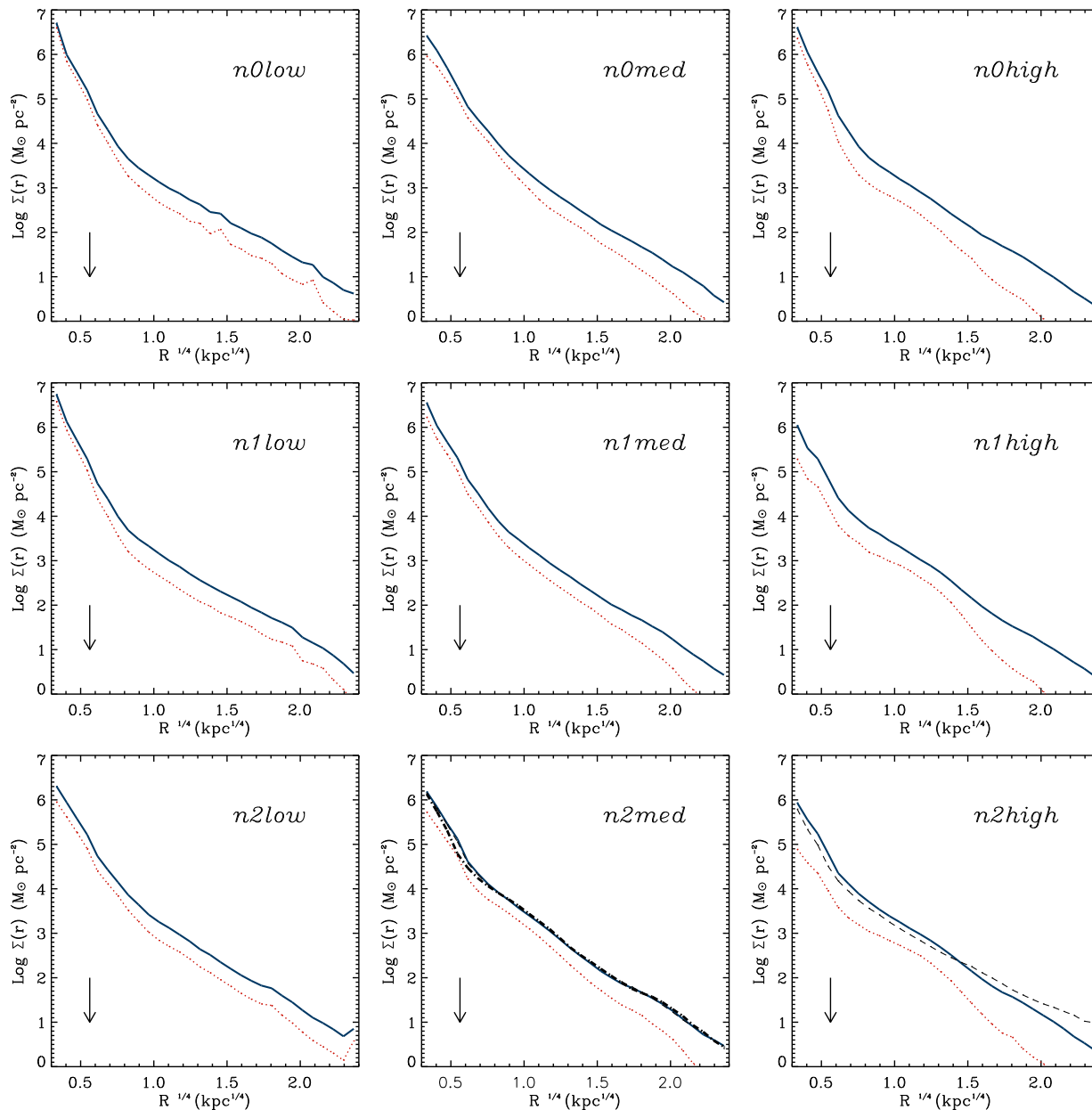


Figure 10. Surface density of each merger remnant projected onto the orbital plane versus the fourth root of the radius. Other projections are qualitatively similar. The solid line is for all stellar mass and the thin dotted line is stellar material formed during the major-merger simulation. The arrow in each plot points to the gravitational softening length of 0.1 kpc. The $n2med$ plot, in the lowest middle panel, also shows the profile of an identical simulation with ten times the resolution and another where gas particles can spawn 10, instead of the standard 2, stellar particles. These variant simulations produce nearly identical profiles. The $n2high$ plot, in the lower right-hand panel, contains a dashed line showing the total stellar profile of a purely collisionless run.

files of 51 merger remnants by Rothberg & Joseph (2004), 16 (30%) had profiles steeper than $r^{1/4}$. Similar studies of ellipticals (Byun et al. 1996) and ULIRGs (Veilleux et al. 2002) have found a much smaller percentage that deviate from $r^{1/4}$ indicating that the discrepancy between the observations and simulations is far from obvious. In fact, during the one Gyr evolution subsequent to the final galaxy merger, the central excess slowly increases due to the remnant gas slowly being converted to stars. This trend might have been abated, or even reversed, if a more violent injection of energy would have dispersed, or removed, the re-

maining gas thereby causing the density profile to remain constant or slightly decrease. While no source of energy is inherent to our feedback model, recent work by Springel et al. (2005a) has shown that an active galactic nucleus (AGN) can indeed expel large amounts of gas and completely shut off star formation. Correlations between mergers and AGN (Veilleux et al. 1995; Wyithe & Loeb 2003) and mergers and outflows (Martin 1999, 2005; Rupke et al. 2005, 2002) provide evidence for this scenario. Moreover, merging black holes at the galactic center could also influence the central stellar distribution (see, e.g., Milosavljević & Merritt

Table 4. Projected remnant properties averaged over 1000 random lines of sight. R_e is the half-mass radius of all stars, while $R_{e,os}$ is the half-mass radius of the old stellar component, both disk and bulge, and $R_{e,ns}$ is the half-mass radius of stars generated during the course of the merger simulation. σ is the velocity dispersion of all the stars measured within half R_e , and σ_5 is the velocity dispersion measured inside an aperture of 5 kpc. The total and new star effective radii are not calculated for the collisionless simulation because there was no star formation included and hence no new stars.

Model	R_e (kpc)	$R_{e,os}$ (kpc)	$R_{e,ns}$ (kpc)	σ (km s ⁻¹)	σ_5 (km s ⁻¹)
<i>n0low</i>	7.4	8.1	6.1	204	212
<i>n0med</i>	3.8	5.7	1.8	263	243
<i>n0high</i>	4.0	6.1	0.8	226	213
<i>n1low</i>	6.8	6.8	6.9	224	231
<i>n1med</i>	3.8	5.8	1.8	263	242
<i>n1high</i>	4.2	5.9	1.9	196	185
<i>n2low</i>	5.9	6.0	5.8	220	224
<i>n2med</i>	4.0	6.0	2.0	232	205
<i>n2high</i>	5.0	6.2	2.3	184	176
collisionless	-	7.2	-	155	155

2001). In a more pessimistic vein, Springel (2005) has recently shown that time integration methods commonly employed in N-body simulation can lead to significant errors when using adaptive timesteps and highly eccentric orbits (see his Fig. 5). Thus, the central densities may be the result of numerical errors which could be remedied by using new codes such as Springel’s GADGET-2. A much more thorough study of the time evolution of the surface density profile, the robustness to numerical integration parameters, and the dependence on various initial conditions will be required to determine if merger remnants evolve into “regular” elliptical galaxies, and if so, which types of ellipticals.

As a final comment, we remark that the centrally concentrated new stellar population present in all models has affected even the collisionless component. The contraction of the collisionless component is clearly demonstrated in the lower-right plot of Figure 10. The total surface density for *n2high* intersects the collisionless profile at $R \approx 4.5$ kpc, signaling that the gaseous dissipation and star formation included in *n2high* has contracted the mass profile in comparison to the collisionless case.

4.4.2 The Fundamental Plane

To begin, we note that the previous section demonstrated that the collisionless stellar distribution responds to gaseous dissipation and star formation in the galaxy center by becoming more concentrated. To quantify the contraction of stellar mass, we measure the half-mass radius R_e of the total, the new, and the old stellar (bulge plus disk) mass and list these in Table 4. The half-mass radius is determined as the radius which encloses half the projected stellar mass. We do not attempt to compute a luminosity profile, nor do we try to fit a $r^{1/4}$ -type luminosity profile since it does not appear

to accurately characterize the surface density. Hence, R_e is not identical to the effective radius, but it serves as a useful proxy. The half-mass radii of the new stars $R_{e,ns}$ shows that half of all stars formed during the medium and high feedback merger simulations end up within ~ 2 kpc of the center of the merger remnant. Further, $R_{e,ns}$ depends on n , the feedback reservoir equation of state index, such that increasing n increases the half-mass radius of the newly formed stellar population. The dissipation, gas infall and star formation has affected the old stars as well. The half-mass radius of the old stars $R_{e,os}$ is $\sim 14 - 20\%$ smaller in the runs including gas, cooling, star formation, and feedback compared to the purely collisionless simulation.

The central concentrations of newly formed stars affect the kinematics of the entire stellar population. To quantify the stellar kinematics, we calculate the one-dimensional velocity dispersion within an aperture centered on the potential minimum. Table 4 lists the velocity dispersion within apertures of radius one-half R_e and 5 kpc, averaged over a thousand projections. The typical scatter due to projection effects is $\sim 10\%$. Because the one-dimensional velocity dispersion is a measure of the depth of the potential well, the remnants with a smaller effective radius naturally lead to a larger velocity dispersion, and in all cases the velocity dispersions are much larger than the collisionless simulation – the largest by over 50%. The dispersion profile also changes. In the collisionless case, the velocity dispersion is flat, i.e., the dispersion is identical when measured within an aperture of 3.6 or 5 kpc. In contrast, the medium and high feedback simulations have a velocity dispersion that increases toward the remnant center.

While we reserve a more extensive study of these merger remnants to future work, it is interesting that the effective radii and velocity dispersions presented in Table 4 are consistent with the early-type R_e - σ scaling relation found in the Sloan Digital Sky Survey (Bernardi et al. 2003, see their Fig. 4 and 5). Further, the differences generated by the feedback models scatter the merger remnants perpendicular to this scaling relation, suggesting that it is the interplay between star formation and feedback which fixes the position of a merger remnant on the fundamental plane of hot stellar systems. The sensitivity of merger remnants to feedback models is potentially a useful discriminator for selecting the best model or parameters.

Figure 10 and $R_{e,ns}$ both demonstrate that the majority of new stars reside within the inner regions of the remnant. This is confirmed in Figure 11, which plots the cumulative mass distribution of new stars in each merger remnant. In all models approximately 80% of *all* new stellar mass is within 10 kpc of the remnant center. In contrast, the simulations of MH96 led to merger remnants in which all of the new stellar material was within 1 kpc of the center. This suggests that our feedback model restricted the gas inflow and dispersed the central star-forming region. The new star mass cumulative profile is highly correlated with n . The $n = 2$ models have the lowest cumulative mass distribution for both the high- and low-feedback series. Apparently, the stiffer equation of state has provided sufficient pressure support for stars to be formed over a larger range of radii, thus decreasing the fraction of stars which reside within the inner ~ 1 kpc of the remnant.

Because stars are stochastically spawned from colli-

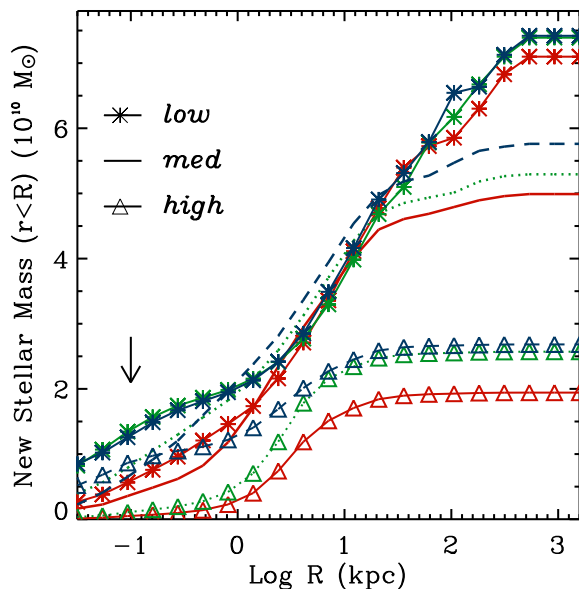


Figure 11. Cumulative new (formed during the merger simulation) stellar mass in the merger remnant for each model. Shown as solid, dotted and dashed thick lines that represent the $n = 2$, $n = 1$, and $n = 0$ feedback models, respectively. Then, the degree of feedback, i.e., *high*, *med*, and *low*, is denoted by the symbols as shown in the key. As in Figure 10, the arrow indicates the gravitational softening length of 0.1 kpc.

sional gas (see the last paragraphs in § 2.2), it is possible that the new stellar component spuriously loses energy and angular momentum due to its artificial coupling to the gas. This was explicitly checked by rerunning the *n2med* simulation with $N_g = 10$, i.e., each gas particle now spawns 10 individual stellar particles as opposed to the fiducial value of 2. The resulting surface-density profile was very similar to *n2med*. The new stars were slightly more extended, with a half-mass radius $R_{e,ns} = 2.2$ kpc, about 10% larger than *n2med*. The more extended new stars also affected the velocity field and the dispersion was lower at half R_e and higher at 5 kpc, but both of these effects were only $\sim 3\%$ of the values listed in Table 4.

5 DISCUSSION

5.1 Convergence Study

The resolution of N-body simulations such as those performed here is determined by the particle number N and the gravitational softening length h . Increasing N and decreasing h both result in higher resolution. Of course, this higher resolution comes at the expense of computational time. In practice, the selection of appropriate values for N and h is a balance between the resolution necessary to address the relevant processes and the available resources. In this section we explore variations in particle number and smoothing length for our fiducial merger simulation. S00 performed a similar study for the isolated disk. To isolate the effect of particle number, we select only one (*n2med*) of the feedback parameters to resimulate with the total particle number increased by factors of 2, 4 and 10. The ratio of dark-matter

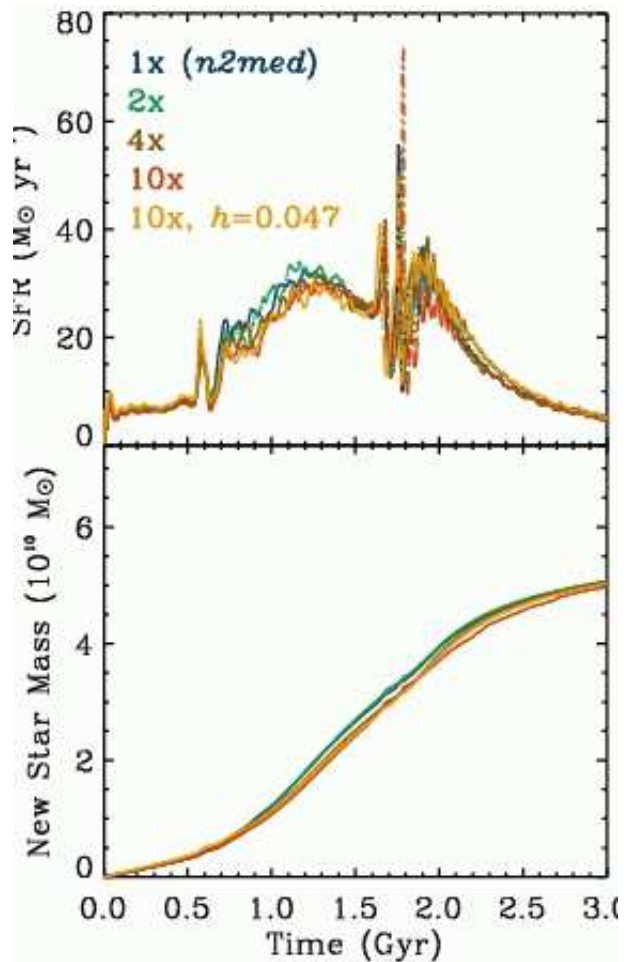


Figure 12. Star-formation rate for our fiducial major merger with runs of varying resolution.

to collisionless disk to collisional particle number remained fixed. The highest resolution simulation contained 1,000,000 dark matter particles, 300,000 each of stellar disk and collisional gas, and 100,000 bulge particles for each galaxy, making the total number of particles used in this simulation 3.4 million. The individual particle masses were $7.1 \times 10^5 M_\odot$ for the dark matter, $1.8 \times 10^5 M_\odot$ for the collisional gas, $1.3 \times 10^5 M_\odot$ for the stellar disk and $1.0 \times 10^5 M_\odot$ for the stellar bulge.

In general, increasing N allows the gravitational softening length to be decreased as roughly $N^{-1/3}$. However, because of the increased computation time resulting from this scaling, we have chosen to use a smaller softening length for only one simulation. We chose our highest resolution simulation that had ten times the particle number. In this case, the softening length was $10^{1/3}$ (0.46) times smaller than the fiducial 0.1 kpc.

Figure 12 shows the star-formation rate for simulations of varied resolution. As the resolution is increased, either via N or h , we find a slight trend of lower star-formation rates during the initial passage, but the effects are less than 5% and, overall, there is excellent agreement between the global gas consumption. The consistency of star formation for all

resolution runs suggests that our fiducial particle number is sufficient to resolve the star-formation history.

The merger remnants are also insensitive to the increased resolution. The surface density, half-mass radii, and velocity dispersions are all within 2% of the *n2med* simulation, with no trend as a function of higher resolution. However, there are subtle differences between the high- and low-resolution simulations. In particular, the number of small condensations orbiting the central gas disk in the merger remnant (see bottom-right panel in Fig. 6) is increased by $\sim 30\%$ in the higher resolution simulation.

5.2 Comparison to Previous Work

The simulations presented here extend prior studies of star formation and feedback in equal-mass gas-rich disk-galaxy major mergers. As in the work of MH96 and S00, we find that mergers drive gas inflows which efficiently form stars and lead to a central concentration of newly formed stellar mass. Furthermore, we have quantified how these results depend on the assumed feedback efficiency and density dependence. However, the comparison to previous work is complicated by the many differences between the methodology used here and that employed in previous work. For clarity and definiteness, we find it useful to enumerate the differences between the simulations presented here and those of MH96 and S00:

(i) To represent stellar feedback, MH96 imparted momentum “kicks” while S00 and this work chose to pressurize the ISM. In a recent paper, Springel et al. (2005b) showed these “kicks” to be a weak form of feedback that was dependent upon the numerical resolution. We do not consider this further.

(ii) Each simulation used a different disk-galaxy model.

(iii) The star-formation recipe employed is identical in all simulations, but the normalization, i.e. the choice of c_* , is different. The fiducial value used in all simulations here was 0.03, while S00 and MH96 both used 0.004. For completeness, we will investigate a range of values both an order of magnitude smaller and larger than ours.

(iv) MH96 represented the ISM as an isothermal gas, at 10^4 K. They argued that gas in disk galaxies efficiently cools and thus fixing the gas to this temperature scarcely affects the gas dynamics. S00 included adiabatic gas processes and shock heating as we do here.

(v) Our simulations use a version of SPH which integrates the entropy, while MH96 and S00 used a version of SPH which integrated the energy.

In order to better understand these differences, we will use this section to describe two types of tests. First, we will build the exact initial conditions of S00 and attempt to duplicate his star-formation history. In addition, we will run his initial conditions with one of our models. In the second series, we use our fiducial model in a number of tests which go through the above items, in order, and resimulate our fiducial *n2med* model with slight modifications aimed at illustrating the outcomes of each assumption. As mentioned above, we do not fully address item (i) because the comparison to the “kicks” feedback used in MH96 has been recently performed by other authors (see Springel et al. 2005b). We

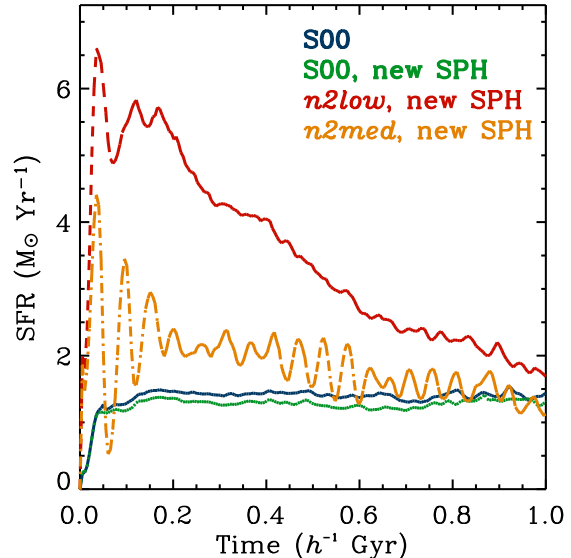


Figure 13. Star formation for model I1 of S00. Shown are four runs, two that have the identical parameters as in S00, which we have labeled accordingly, and the final two runs use the *n2low* and *n2med* parameters used throughout this work. Because the original work of S00 used the “energy, standard” formulation of SPH, our primary comparison run uses this as well. The other two runs use the newer version which is the standard for the main body of this paper.

also do not perform a full exploration of the second difference listed above, the disk galaxy model. A complete understanding of the dependencies associated with the initial conditions is outside the scope of this work (the beginning of such a project was broached in Cox (2004)). However, our first type of test, the explicit comparison using the models of S00, will suffice to provide a basic understanding of item (ii) above.

5.2.1 Comparison to S00

As a first task we’ll verify that our model can reproduce one of the quiescent star-formation histories and one of the merging disk-galaxy star-formation histories previously shown in S00. In order to perform this test, we must construct identical initial disk models to those used in S00. As a byproduct of this test, we will gain some insight as to how the disk galaxy model determines the resulting star-formation history.

For the isolated galaxy comparison, we choose the I1 galaxy model outlined in § 4.1 of S00. This model has $V_{200} = 160$ km s $^{-1}$, and thus a virial mass of $1.4 \times 10^{12} M_{\odot}$. The halo has a concentration $c = 5$ and a spin parameter $\lambda = 0.05$. All of the baryons are in a disk, i.e., there is no bulge component, and 20% of the baryons are in a gaseous form. This results in mass fractions of $m_d = 0.04$, $m_g = 0.01$, and $f_d = 0.2$. Further, the gas and stellar disks are assumed to follow the same exponential distribution (i.e., $\alpha = 1$) with a radial disk scale length of 6.4 kpc. The model is realized with 30,000 dark matter, 20,000 gas and 20,000 stellar disk particles for the same resolution used in S00.

When we introduced the parameter sets in § 2.5 we

provided the conversion to the exact model used in S00. This parameter set had a lower star formation normalization $c_\star = 0.004$, but was otherwise very similar to our *n2low*. Although this wasn't used for any of the models thus far, we now use it to simulate the galaxy model I1 in isolation. It is also significant to point out that the original S00 simulations used the “energy, standard” formulation of SPH where we have used a newer version introduced by Springel & Hernquist (2002). We will simulate the S00 parameter set with both here. As a reference to the parameter sets we've developed in this work, we will also run the I1 model with the *n2low* and *n2med* parameter sets.

Figure 13 shows the resulting star formation for the I1 galaxy model evolved 1.4 Gyr. As a confirmation of our ability to replicate the initial disk model, we note that both of the simulations that used the S00 parameter set have star-formation histories that are nearly identical to that shown in S00 (see his Fig. 7). Since the only difference between these two runs is the version of SPH, we conclude that the version of SPH makes little difference for evolving disk galaxies in isolation.

The two simulations which evolved I1 with the *n2low* or *n2med* parameter set are quite different. The *n2low* model has a much higher star formation rate because it is nearly identical to S00, only it has a larger value of c_\star . Because of this, nearly three times as much gas is converted to stars during the simulation and this rapid star formation quickly depletes the disk of high-density gas resulting in an sub-sequential decline of the star-formation rate. The average star-formation rate of the simulation that uses the *n2med* parameter set is much closer to that of the S00 runs, however there are strong oscillations present. These oscillations were seen in the med- and high-feedback runs during the Sbc major merger and were discussed briefly at the end of § 4.1

An interesting comparison can be made between the star formation reported in Figure 13 for the isolated I1 disk, and that shown earlier in Figure 1 for the isolated Sbc disk. First, with the *n2low* parameter set, we note that the Sbc disk has a steady star-formation rate of $\sim 0.75 M_\odot \text{yr}^{-1}$. This same parameter set for the I1 disk begins with a much larger star-formation rate ($\sim 6 M_\odot \text{yr}^{-1}$) that quickly declines as the high-density gas is consumed. Not surprisingly, one concludes that the star-formation history is a direct consequence of the amount and distribution of high-density gas, both of which are a byproduct of the initial disk model (see also Li et al. 2005, 2006; Springel et al. 2005b). This leads us to suggest a natural extension to our work: extend our tests to a large set of initial disk models with properties drawn from observations, as with our Sbc-disk model. By comparing these tests to observed relations between Hubble-type and star formation, one may provide further constraints on the star formation and feedback model.

After assuring ourselves that we are able to evolve the exact I1 model of S00 in a similar fashion and investigating the differences induced by either the version of SPH, or the alternate star formation and feedback model, we now move on to test one of his major mergers. For this test, we select the bulgeless A1 major merger. These initial disk models are slightly smaller than the I1 disk, with $V_{200} = 120 \text{ km s}^{-1}$, and thus their mass is $6.0 \times 10^{11} M_\odot$. The halo has a concentration $c = 5$ and a spin parameter $\lambda = 0.05$. As with

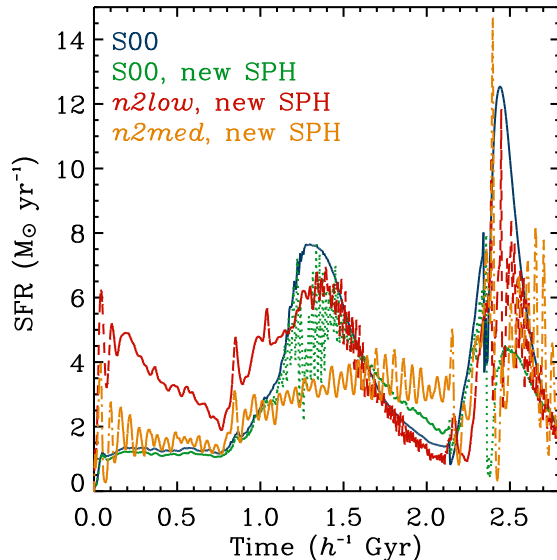


Figure 14. Star formation for the A1 bulgeless major merger of S00. As with Figure 13, we show one run that is designed to reproduce the star-formation history of S00, and three other runs which have small variants in either the star formation and feedback parameters, or the version of SPH.

the I1 model, all of the baryons are in a disk, i.e., there is no bulge component, and the mass fractions are $m_d = 0.04$ and $m_g = 0.01$, where the gaseous and stellar disks are similarly distributed. This model is realized with an identical particle number as I1.

Figure 14 shows the star formation rate for the A1 major merger. As with the I1 test, we run four simulations: one identical to S00, one with the same star formation and feedback parameters as S00 but with the newer version of SPH, and two with our parameter sets *n2low* and *n2med*. Once again, when we use the S00 parameter set and the identical version of SPH, we can reproduce the A1 merger star-formation rate exactly (see Fig. 14 of S00).

In contrast to the isolated case, when we use the S00 parameter set with the newer version of SPH, the star-formation history shows marked changes. The star-formation rate in this case is oscillatory and suppressed relative to the S00 result. These changes occur primarily during the bursts of star formation that result after the first passage and the final merger and are likely a result of the improved entropy conservation in the newer version of SPH. We will perform more tests along this line, and discuss this further in § 5.2.5

The other two runs, which use the *n2low* and *n2med* parameter sets, also show distinct differences from S00. As in the case of the isolated disk, *n2low* shows much larger star formation during the quiescent stages of evolution. However, the bursts are relatively similar in amplitude, especially to the S00 model with the same SPH version. The *n2med* run shows the oscillations that were also present in I1 and Sbc, and there is almost no burst of star formation subsequent to the first passage at $T = 1.0 - 1.7 h^{-1} \text{ Gyr}$. The final merger, however, contains the highest star-formation rate of any of the four models.

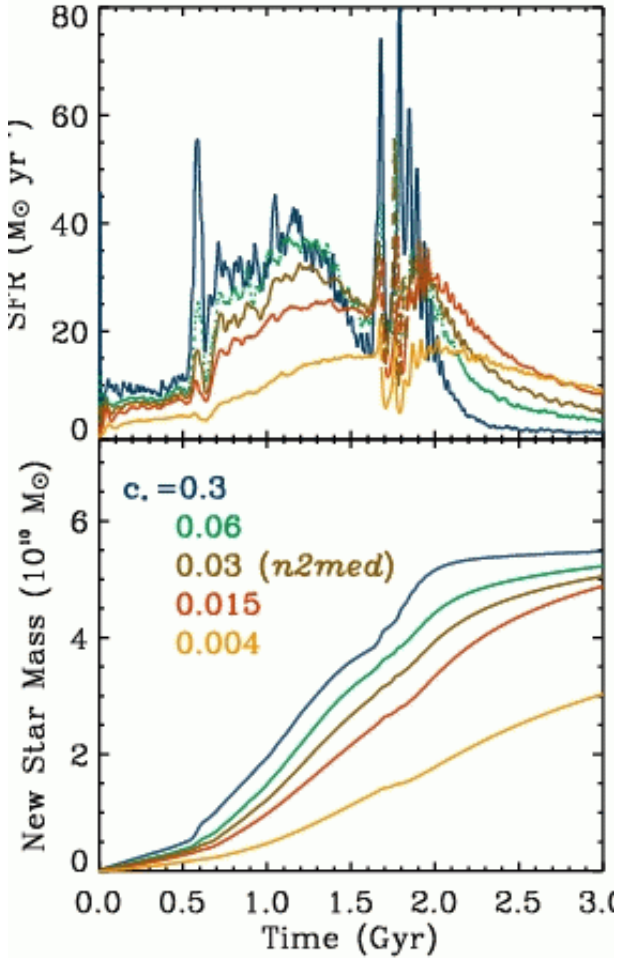


Figure 15. Star-formation rate during the fiducial merger for different values of c_* , the parameter that sets the star formation efficiency.

From the tests performed in this section, we arrive at three primary conclusions. First and foremost, our model reduces to that of S00, and as such, if we use his initial conditions, we can reproduce his results. Second, we note that the increased value for the star-formation normalization c_* , unsurprisingly, produces an increased star-formation rate. This increase occurs only during the quiescent evolution. During the merger-induced bursts, the star-formation rate is nearly equivalent, as demonstrated in Figure 14. The third conclusion pertains to the version of SPH. While this made very little difference while evolving the quiescent disk, there are substantial differences that occur during the more dynamic merger. We will perform a more thorough exploration of these last two dependencies, c_* and the version of SPH, using our Sbc disk-galaxy model in the sections that follow.

5.2.2 Star-Formation Recipe: Normalization

The parameter c_* normalizes the course-grained recipe to convert gas to stars via Equation (1). While §4.1 showed that $c_* = 0.03$ reproduced the observational Kennicutt law (2) over two orders of magnitude in gas surface density, the

Table 5. Star-formation properties of major merger simulations as a function of c_* . Quantities are defined in Table 3.

c_*	e	SFR _{max} ($M_\odot \text{ yr}^{-1}$)	T_{LIRG} (Gyr)
0.3	0.51	82	1.30
0.06	0.49	57	1.36
0.03 (<i>n2med</i>)	0.47	56	1.34
0.015	0.45	38	1.21
0.004	0.28	22	0.01

observational scatter appears large enough to allow for a range of star-formation efficiencies. In this section, we resimulate the fiducial *n2med* model with $c_* = 0.004, 0.015, 0.06,$ and 0.3 . These values of c_* represent excursions from our fiducial value (0.03) of an order of magnitude (0.004 and 0.3) and a factor of two (0.015 and 0.06). Both MH96 and S00 used $c_* \approx 0.004$.

Figure 15 shows the star-formation rate for the fiducial *n2med* simulation and the four mergers with alternate star-formation normalizations. Not surprisingly, the star formation prior to the final merger correlates with the star formation efficiency c_* , but the situation reverses after the merger. In fact, the low efficiency of star formation means very little gas is consumed prior to the final merger, and by the end of the simulation, at $T = 3.0$ Gyr, the $c_* = 0.004$ simulation has the highest rate of star formation. In a manner similar to §4.1, the star formation can be quantified by the gas consumption, the maximum star-formation rate, and the duration in which the merger would qualify as a LIRG, which are listed in Table 5.

Varying the star-formation efficiency highlights the differing effects of star formation versus feedback. For example, changing the fiducial *n2med* model by decreasing c_* to 0.004 (as done above) or increasing τ_{fb} to 2.0 (*n2high*), reduces SFR_{max} and e . Increasing the feedback, as in *n2high*, restricts the ability of gas to reach high densities, but gas which does so will be rapidly converted to stars. Hence, the gas consumption e is strongly affected while the peak star-formation rate is only slightly less than *n2med*. In contrast, decreasing c_* only slightly alters the gas density but strongly reduces the star-formation efficiency of the high-density gas. In this case, the maximum star-formation rate is less than half *n2med*, but the gas consumption e is higher than when increasing the feedback.

Because the star-formation rate was affected by different values of the star-formation efficiency c_* , it's reasonable to ask if the agreement with the Kennicutt law has been destroyed. Figure 16 answers this question by showing the gas and star-formation rate surface densities in a 2 kpc aperture for each of the simulations with different c_* . As expected, due to our coupling of star formation to the gas density via Equation (1), the slope of each simulation tracks the observed Kennicutt law. However, the various normalizations have shifted the amplitude of star formation so that the values 0.3, and 0.004 are on the edges of the observed range.

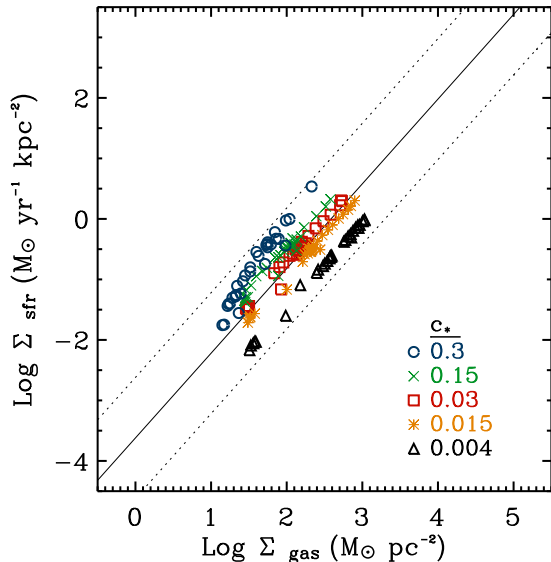


Figure 16. Identical to Figures 8 except shown here are simulations with varying star-formation normalization c_* . The (red) squares are the fiducial *n2med* simulation and were similarly shown in Figure 8. The (blue) circle, (orange) asterisk, (yellow) cross, and (black) triangle symbols are for $c_* = 0.3, 0.06, 0.015$, and 0.004 , respectively.

5.2.3 Star-Formation Recipe: Slope

The previous section demonstrated that the normalization of the projected star-formation law, and hence the agreement with Kennicutt (1998), is set by the free parameter c_* . However, we have still not demonstrated what sets the slope of the star-formation law. Previous efforts have argued that the observed star-formation law is a natural consequence of the turbulent interstellar medium (Kravtsov 2003) or that it results from gravitational instabilities in gaseous spiral disks (Li et al. 2004). In order to investigate the origin of the slope of the star-formation law, we will follow a procedure similar to Mihos et al. (1991) and modify our star-formation prescription, i.e., Equation (1). To this end, we write a generalized star-formation law as

$$\frac{d\rho_*}{dt} = C\rho_{\text{gas}}^N, \quad (23)$$

where C is a dimensionful free parameter and N sets the gas-density power-law dependence. In our fiducial model, $C = \sqrt{4\pi G}c_*$, and $N = 1.5$. As variants, we will try $N = 0$ and 2 , and fix C such that the global star-formation rate is identical at ρ_{th} . To simplify the comparison, we only show results from simulations where the star formation is not fixed to be zero below ρ_{th} . We also performed identical simulations that included the threshold density, however in this case the star-formation surface density quickly plunged to zero below $\sim 10 \text{ M}_\odot \text{ pc}^{-2}$, as in Figure 3, and thus there was very little difference between the various star-formation laws.

Figure 17 shows the star-formation law for our isolated Sbc disk galaxy for the three variants of the star formation prescription. We see a clear trend that the slope of the projected star-formation law follows the power of N in Equation (23). This correlation was also noted by Mihos et al.

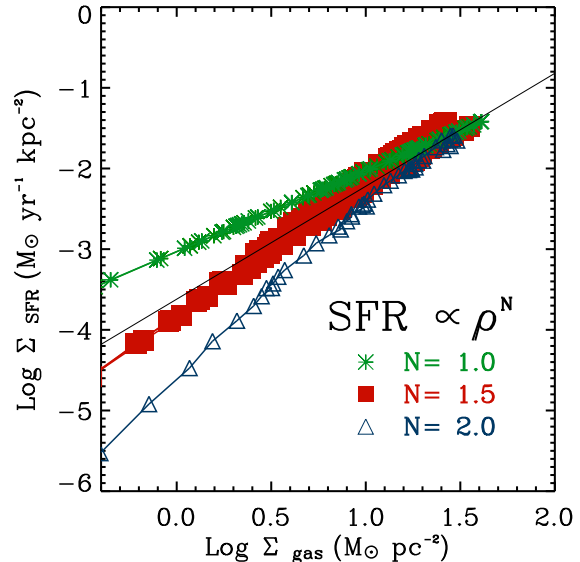


Figure 17. This figure is identical to Figure 3 except here we compare our fiducial *n2low* model to variants that have an altered star-formation law according to Equation (23), with $N = 0, 2$ (opposed to the fiducial $N = 1.5$). All simulations are run with the threshold density for star-formation set to zero.

(1991), who additionally showed that the steeper powers of N result in starbursts of greater intensity. From these considerations we conclude that the star-formation law, both in normalization and slope, is fixed by the empirical Kennicutt law.

5.2.4 Isothermal ISM

Next we consider differences generated by assuming the ISM is an isothermal gas with temperature 10^4 K . Because of the efficient cooling in quiescent disk galaxies, it is reasonable to assume their thermal energy is maintained near 10^4 K . Indeed, this is precisely the case for our model galaxy when simulated in isolation, there is no difference.

However, galaxy mergers are a much more violent event in which there is ample shock heating of low-density gas (Cox et al. 2004). This was demonstrated in §4.3, where phase diagrams showed large amounts of hot ($\sim 10^6 \text{ K}$), low density ($10^{-4} - 10^{-7} \text{ M}_\odot \text{ pc}^{-3}$) gas. In this state, the cooling time is much longer than the orbital time, and the gas becomes locked in this phase, unable to cool. If the temperature of this gas were fixed at 10^4 K , this gas would be much more likely to fall back to the galactic center and could significantly affect the star-formation rate.

To investigate this possibility, we have run our *n2med* model with the *thermal* gas temperature (the u reservoir) fixed to 10^4 K . (In order to maintain a stable isolated disk, the feedback reservoir q still operates normally.) Under these assumptions, the star-forming gas is scarcely different than *n2med* while all non-star forming gas is effectively 10^4 K , without gas which has recently formed stars and hasn't thermalized its turbulent energy yet. The resulting star formation, in comparison to *n2med*, is shown in Figure 18. The isothermal assumption results in a maximum star-formation

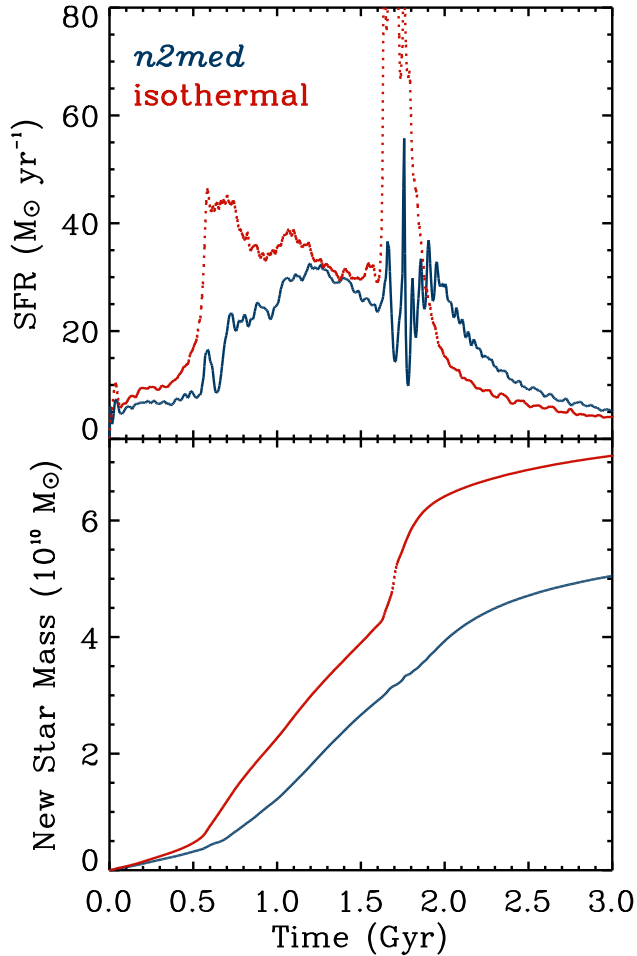


Figure 18. Star-formation rate for our *n2med* model and for the identical model except the temperature of non-star forming gas is fixed at 10^4 K.

rate that is four times that of *n2med* and increases the gas consumption e by 20% over *n2med*. This gas fraction is nearly identical to the quantity of gas which ends up in the hot, low-density phase in *n2med*. Further, the periods of maximum difference between the two star-formation rates is precisely when large shock heating occurs. It thus appears that assuming the ISM is isothermal at 10^4 K grossly underpredicts the amount of shock heating due to the merger and results in much more cold gas available for star formation.

5.2.5 SPH Version

All simulations presented up to this point have used a version of SPH which integrates the entropy and was formulated to conserve both energy and entropy, when appropriate (Springel & Hernquist 2002). In order to discern the effects of our choice of SPH we resimulate the fiducial *n2med* merger with alternate versions. Specifically, we use the energy integrating “energy, geometric”, “energy, standard”, and “energy, asymmetric” versions of SPH, as well as the entropy integrating “entropy, standard” version, where we follow the naming convention of Springel & Hernquist (2002) and refer the interested reader to their paper for further de-

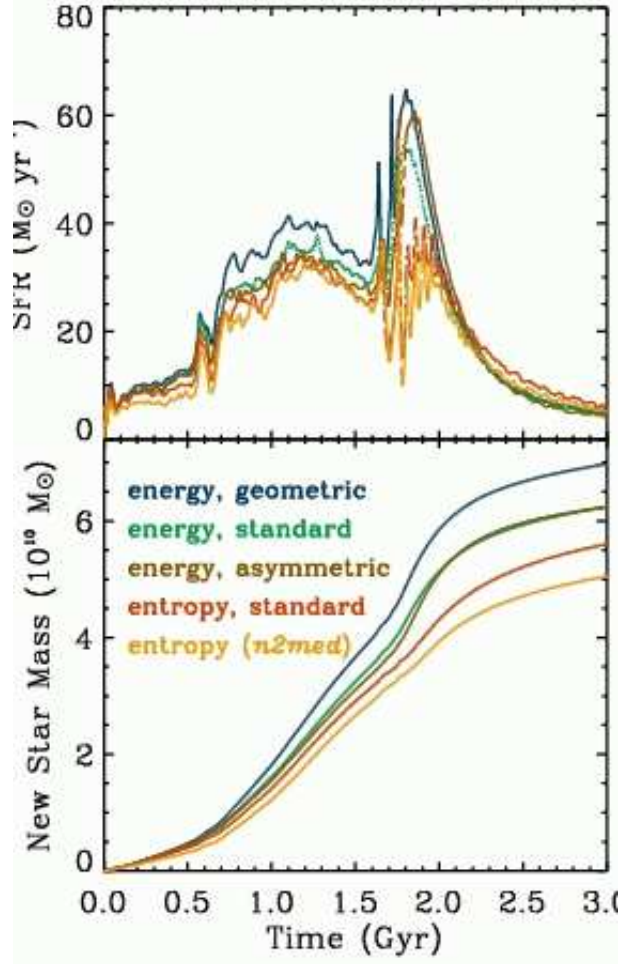


Figure 19. A comparison of our fiducial *n2med* model run with different versions of SPH commonly used in numerical simulations.

Table 6. Star formation properties of major merger simulations as a function of SPH formulation. Quantities are defined in Table 3.

SPH Version	e	SFR_{max} ($M_{\odot} \text{ yr}^{-1}$)	T_{LIRG} (Gyr)
entropy (<i>n2med</i>)	0.47	56	1.34
energy, standard	0.58	55	1.48
energy, geometric	0.65	65	1.52
energy, asymmetric	0.58	61	1.42
entropy, standard	0.52	60	1.38

tails. The galaxy-merger simulations of S00 and MH96 used the “energy, standard” version.

Figure 19 shows the star-formation rate during the SPH runs. There are two notable features present in the star-formation histories owing to the version of SPH. The first feature is the systematic enhancement of star formation from $T = 0.6$ to 1.6 Gyr in runs that do not use the fiducial Springel & Hernquist (2002) version of SPH. The second feature is present after the final merger, from $T = 1.8$ to 2.0 Gyr, when the energy versions of SPH lead

Table 7. Star formation properties of major merger simulations as a function of ISM metallicity. The metallicity is given relative to solar and the remaining quantities are defined in Table 3.

Metallicity (Z_{\odot})	e	SFR_{max} ($M_{\odot} \text{ yr}^{-1}$)	T_{LIRG} (Gyr)
zero (<i>n2med</i>)	0.47	56	1.34
10^{-3}	0.49	54	1.38
10^{-2}	0.50	54	1.40
$10^{-1.5}$	0.54	47	1.44
10^{-1}	0.58	67	1.44
1	0.60	53	1.52

to a large peak of star formation while the entropy versions (*n2med* and “entropy, standard”) of SPH have an oscillatory star-formation rate. In general, the entropy versions lead to lower star-formation rates and less gas consumption. We speculate that these features arise because the entropy versions of SPH more accurately treat point-like energy injections and adiabatic heating as gas falls into the central region of the halo, as demonstrated in Springel & Hernquist (2002), and therefore may be more accurate than energy versions of SPH. Additionally, while versions of SPH not tested here may produce still different results, we feel that the tests performed here survey the plausible range of outcomes and accurately reflect the modeling uncertainties resulting from versions SPH.

While these tests show that the version of SPH can alter the star formation during a galaxy interaction, we note that these differences are smaller than differences induced by other modeling assumptions. For instance, Table 6 shows that the total amount of gas consumed and maximum star-formation rate for this series of mergers varies by $< 20\%$. By comparison, changes in the star formation efficiency (c_*) or feedback parameters (τ_{fb} and n) can produce differences of over a factor of 2 (see Tables 3 and 5).

5.3 ISM Metallicity

The ISM radiatively cools at a rate which is highly dependent upon the metallicity. Up to now, cooling has been calculated assuming the ISM is a primordial plasma with zero metallicity even though metals are tracked by the code, as mentioned in § 2.3. In this section we resimulate the fiducial *n2med* model with radiative cooling calculated from the tabulated cooling curves of Sutherland & Dopita (1993) and assumed gas metallicities, in units of solar, of 10^{-3} , 10^{-2} , $10^{-1.5}$, 10^{-1} , and 1. As with our fiducial model, we continue to ignore spatial and temporal changes in the metallicity. The resulting star-formation rate is shown in Figure 20. As expected, the increased metallicity leads to a higher fraction of the gas in the cold phase, and increases the star-formation rate. The more efficient metal-line cooling is strongest for gas which is $\sim 10^5$ K, and hence the star formation differences are not apparent until gas begins to populate this temperature range. Gas at these temperatures is produced by the interaction itself, in shocks that occur between gas in the progenitor disks. While the maximum star-formation rate does not dramatically change for simulations with increased gas metallicity, the gas consumption e steadily increases. In

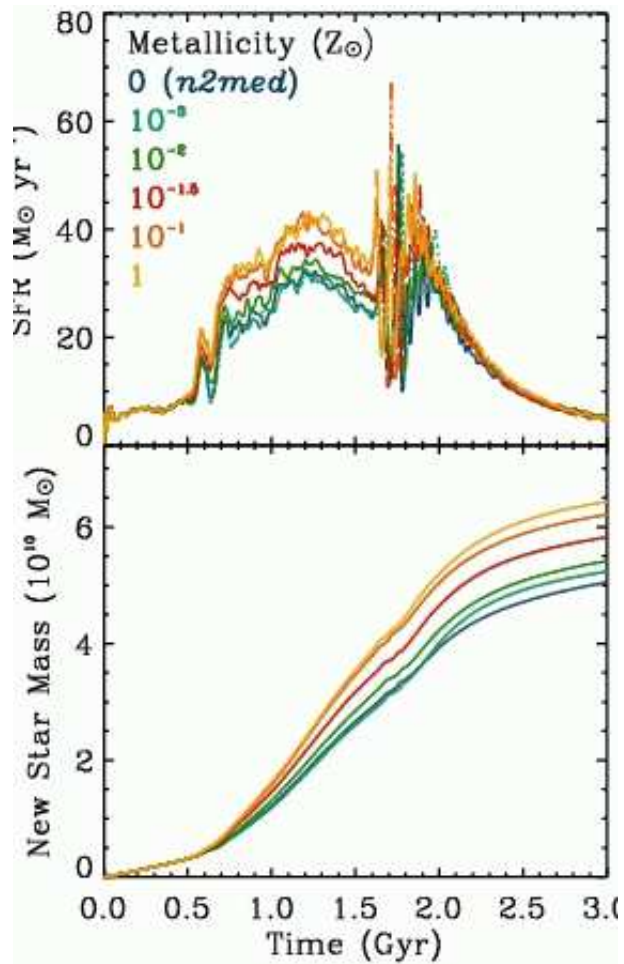


Figure 20. Star-formation rate for our fiducial major merger with various assumptions for the inter stellar medium metallicity. The metallicities listed are in solar units.

fact, there is a 13% increase in e during the merger with solar versus zero metallicity. The star-formation properties are listed in Table 7.

The variations in gas consumption suggest that appreciable errors can be generated when numerical simulations treat the ISM as a primordial plasma. While these variations are smaller than those induced by altering the star formation and feedback parameters (see Tables 3 and 5) the cooling rate can be calculated fully self-consistently because the simulation tracks metal enrichment (see §2.3). Toward this end a number of groups have recently included metallicity-dependent cooling based upon a model for the enrichment of metals from supernovae (SN) (see, e.g., Scannapieco et al. 2005, 2006; Okamoto et al. 2005; Tornatore et al. 2004; Mosconi et al. 2001) and have found similar trends to those reported here. Unfortunately, these models necessarily require a number of assumptions regarding the time delay of SNIa, the physical scale that stellar particles distribute their metals, the diffusion of metals, and the scale in which metals are smoothed when the cooling is calculated. At the current moment it is unclear how best to implement the physics of metal enrichment and metallicity-dependent cooling but these physical processes are certain to garner a significant amount of attention in the near future.

6 CONCLUSION

We have carried out a series of isolated and merging disk galaxy simulations which include simple recipes for implementing star formation and feedback. The free parameters of these models are selected based upon the stability of our isolated disk galaxy model and excursions are explored with increased and decreased stability. These models were then used during equal-mass prograde major mergers to investigate the resulting star-formation and remnant properties. The primary conclusions can be summarized as follows:

- The slope and normalization of the star-formation law are fixed by adopting a recipe in which stars are formed from high-density gas according to $\dot{\rho}_* \approx c_* \rho_{\text{gas}}^{1.5}$. The slope is a result of the 1.5 index, and the normalization is set by c_* . Star formation designed in this manner, independent of the feedback model, can naturally reproduce the empirical Kennicutt law. The above holds for both quiescent and interacting galaxies.

- Provided that star formation is designed as in the first item above, the rate at which stars are formed is then determined by the feedback efficiency τ_{fb} . The star-formation rate in isolated disk galaxy simulations is largely insensitive to the equation of state at high densities (in our model this is controlled by n), because any feedback sufficient to stabilize the galactic disk is also efficient enough to confine star-forming gas to a narrow range of densities around the threshold density ρ_{th} .

- During a merger, where gas can achieve much higher densities than in the isolated case, the star formation rate depends on both τ_{fb} and n . However, the overall gas consumption is fixed primarily by τ_{fb} , the feedback efficiency. Because τ_{fb} determines the pressurization of star-forming regions around the threshold density, large values can prevent gas from ever reaching star-forming densities.

- The maximum star-formation rate during the merger simulations depends on τ_{fb} in a way which is reasonably well approximated by a toy model of star-forming gas in a fixed potential (Equation 22).

Our results extend, and are consistent with, previous numerical simulations of star formation in colliding disk galaxies. A detailed comparison finds that previous versions of SPH predict an increased gas consumption by varying amounts. We also determined that an isothermal gas assumption at 10^4 K also predicts much more efficient star formation during a major merger.

The above items collectively imply that requiring free parameters to yield a stable isolated disk and star formation that is consistent with the Kennicutt law provides a fairly tight constraint on the star-formation recipe but does not uniquely determine the feedback parameters. The large amount of freedom in selecting the feedback parameters makes a significant difference to the maximum star-formation rate during a galaxy merger, while still fulfilling these basic requirements.

Generally speaking, the integrated gas consumption during a merger is less sensitive to the details of the feedback parameters, due to a trade-off between star-formation rate and the duration of the burst. In models with highly efficient feedback, strong bursts of star-formation are suppressed. However, star formation then continues until all the

gas at star-forming densities has been consumed, leading to a similar overall gas consumption.

While we argue that the formulation of star formation in the numerical simulations is well defined, the determination of the feedback parameters is not and thus we ask the question: Is there any hope of determining a unique set of feedback parameters which may then be used for a large series of galaxy merger simulations? In our (optimistic) opinion, the answer to this question is yes. However, doing so may be a long, arduous, and ill-defined process. As a first step we note that there is a strong observational link between galaxy interactions and star formation (e.g., Borne et al. 2000; Lambas et al. 2003; Barton Gillespie et al. 2003; Nikolic et al. 2004). Theoretically, models of galaxy formation with merger induced star-formation naturally produce the Lyman-break galaxies (Somerville et al. 2001) and possibly also submillimeter galaxies (Baugh et al. 2005). Thus, it seems reasonable to require that our merging gas-rich spiral galaxies induce a significant burst of star formation. In this sense, the “high” feedback models are disfavored. Further constraints on burst strengths and ages may place tighter bounds on feedback models. For instance, the prolonged bursts present in the $n = 2$ models may be at odds with observations that suggest starburst have a shorter duration ~ 100 Myr. We also note that it would be very helpful to have a statistical observational catalog of mergers and merger remnants, including estimates of the orbits and galaxy masses, burst strengths and ages, and any associated kinematics to compare with the simulations.

Ultimately, one of the most promising tests of star formation and feedback models may require detailed comparisons between observations of quiescent or interacting galaxies and simulations designed to reproduce these galactic systems. Modeling of specific galaxy systems has already been done in several instances such as “The Mice” (Barnes 2004), M51 (Salo & Laurikainen 2000), Arp118 (Lamb et al. 1998), Arp119 (Hearn & Lamb 2001), Arp220 (McDowell et al. 2003), NGC 7714/15 (Struck & Smith 2003; Smith et al. 2005), NGC 2442 (Mihos & Bothun 1997), IC2163/NGC 2207 (Struck et al. 2005) and NGC 7252 (Hibbard & Mihos 1995), although none of these explored a range of feedback parameterizations. It is evident that much work must be done to determine what initial conditions are plausible and which physical processes must be included to reproduce the varied and extreme environments of galaxy mergers.

Even with the ambiguities present in our models it is encouraging that under a wide range of assumptions we are able to produce stable, gas-rich quiescent galaxies and large prolonged bursts of star formation. Furthermore, for the models that produce large bursts of star formation, the insensitivity of the global gas consumption to the details of the model leads us to believe that we can apply these techniques to a large series of minor as well as major merger simulations and achieve a reliable estimate of the ability of galaxy interactions to drive star formation, a project which has already been started. While the same universality does not hold for the maximum star-formation rate of each model, this is something that might allow us to constrain feedback by matching to observations, as we mentioned above.

In addition, we have presented evidence that the remnant properties, such as half-mass radius and velocity disper-

sion, are highly dependent upon the star formation and feedback assumptions. Low feedback models are more concentrated and have higher central velocity dispersions. Hence, it is likely that performing a large series of runs, and comparing them to a statistical sample of elliptical galaxies, will significantly discriminate between the models. It is also possible that some leverage can be garnered from the significant differences in gas properties predicted by the different feedback models. By comparing phase diagrams such as those in §4.3 to mass-weighted phase diagrams of observed galaxies there may be some models that could be ruled out. Another avenue for comparison between the models and observations is the gas morphology. For instance, the feedback parameters affect the vertical structure of the gas disk, and hence quantities like the inclination dependence of dust attenuation (Jonsson 2004).

ACKNOWLEDGMENTS

We thank Volker Springel for very useful comments and for making GADGET and his initial conditions generator available to us. We also thank Anthony Aguirre, Avishai Dekel, and Jennifer Lotz for a careful reading of a prior version of this paper. This research used computational resources of the National Energy Research Scientific Computing Center (NERSC), which is supported by the Office of Science of the US Department of Energy and also UpsAnd, a Beowulf at UCSC supported by NSF. T.J.C. and J.R.P. were supported by grants from NASA and NSF, and P.J. is supported by HST-AR-10678.01-A, provided by NASA through a grant from the Space Telescope Science Institute, which is operated by the Association of Universities for Research in Astronomy, Incorporated, under NASA contract NAS5-26555. P.J. also acknowledges support by grants from IGPP/LLNL.

REFERENCES

- Balcells M., Graham A. W., Domínguez-Palmero L., Peletier R. F., 2003, *ApJL*, 582, L79
- Barnes J. E., 1992, *ApJ*, 393, 484
- Barnes J. E., 2002, *MNRAS*, 333, 481
- Barnes J. E., 2004, *MNRAS*, 350, 798
- Barnes J. E., Hernquist L., 1996, *ApJ*, 471, 115
- Barnes J. E., Hernquist L. E., 1991, *ApJL*, 370, L65
- Barton Gillespie E., Geller M. J., Kenyon S. J., 2003, *ApJ*, 582, 668
- Baugh C. M., Lacey C. G., Frenk C. S., Granato G. L., Silva L., Bressan A., Benson A. J., Cole S., 2005, *MNRAS*, 356, 1191
- Bekki K., 1998, *ApJ*, 496, 713
- Bekki K., Shioya Y., 1997, *ApJL*, 478, L17+
- Bekki K., Shioya Y., 1998, *ApJ*, 497, 108
- Bell E. F., de Jong R. S., 2001, *ApJ*, 550, 212
- Bender R., Burstein D., Faber S. M., 1992, *ApJ*, 399, 462
- Bernardi M., Sheth R. K., Annis J., Burles S., Eisenstein D. J., Finkbeiner D. P., Hogg D. W., Lupton R. H., Schlegel D. J., SubbaRao M., Bahcall N. A., Blakeslee J. P., Brinkmann J., Castander F. J., Connolly A. J., Csabai I., Doi M., Fukugita M., Frieman J., Heckman T., Hennessy G. S., Ivezić Ž., Knapp G. R., Lamb D. Q., McKay T., Munn J. A., Nichol R., Okamura S., Schneider D. P., Thakar A. R., York D. G., 2003a, *AJ*, 125, 1866
- Bernardi M., Sheth R. K., Annis J., Burles S., Eisenstein D. J., Finkbeiner D. P., Hogg D. W., Lupton R. H., Schlegel D. J., SubbaRao M., Bahcall N. A., Blakeslee J. P., Brinkmann J., Castander F. J., Connolly A. J., Csabai I., Doi M., Fukugita M., Frieman J., Heckman T., Hennessy G. S., Ivezić Ž., Knapp G. R., Lamb D. Q., McKay T., Munn J. A., Nichol R., Okamura S., Schneider D. P., Thakar A. R., York D. G., 2003b, *AJ*, 125, 1849
- Binney J., Tremaine S., 1987, *Galactic dynamics*. Princeton, NJ, Princeton University Press, 1987, 747 p.
- Blumenthal G. R., Faber S. M., Primack J. R., Rees M. J., 1984, *Nature*, 311, 517
- Borne K. D., Bushouse H., Lucas R. A., Colina L., 2000, *ApJL*, 529, L77
- Bottema R., 1993, *A&A*, 275, 16
- Bottema R., 2003, *MNRAS*, 344, 358
- Boylan-Kolchin M., Ma C.-P., Quataert E., 2005, *MNRAS*, 362, 184
- Boylan-Kolchin M., Ma C.-P., Quataert E., 2006, *MNRAS*, 369, 1081
- Broeils A. H., van Woerden H., 1994, *A&AS*, 107, 129
- Bullock J. S., Dekel A., Kolatt T. S., Kravtsov A. V., Klypin A. A., Porciani C., Primack J. R., 2001, *ApJ*, 555, 240
- Byun Y.-I., Grillmair C. J., Faber S. M., Ajhar E. A., Dressler A., Kormendy J., Lauer T. R., Richstone D., Tremaine S., 1996, *AJ*, 111, 1889
- Cole S., Lacey C. G., Baugh C. M., Frenk C. S., 2000, *MNRAS*, 319, 168
- Cox T. J., 2004, PhD thesis, UC Santa Cruz, <http://physics.ucsc.edu/tj/work/thesis>
- Cox T. J., Di Matteo T., Hernquist L., Hopkins P. F., Robertson B., Springel V., 2006, *ApJ*, 643, 692
- Cox T. J., Dutta S., Di Matteo T., Hernquist L., Hopkins P. F., Robertson B., Springel V., 2006, *arXiv:astro-ph/06xxxxx*
- Cox T. J., Primack J., Jonsson P., Somerville R. S., 2004, *ApJL*, 607, L87
- Dantas C. C., Capelato H. V., Ribeiro A. L. B., de Carvalho R. R., 2003, *MNRAS*, 340, 398
- de Jong R. S., 1996, *A&A*, 313, 45
- Dekel A., Cox T. J., 2006, *MNRAS*, 370, 1445
- Dekel A., Stoehr F., Mamon G. A., Cox T. J., Novak G. S., Primack J. R., 2005, *Nature*, 437, 707
- Djorgovski S., Davis M., 1987, *ApJ*, 313, 59
- Dressler A., Lynden-Bell D., Burstein D., Davies R. L., Faber S. M., Terlevich R., Wegner G., 1987, *ApJ*, 313, 42
- Duc P.-A., Bournaud F., Masset F., 2004, *A&A*, 427, 803
- Flores R., Primack J. R., Blumenthal G. R., Faber S. M., 1993, *ApJ*, 412, 443
- Gerritsen J. P. E., Icke V., 1997, *A&A*, 325, 972
- Gnedin O. Y., Kravtsov A. V., Klypin A. A., Nagai D., 2004, *ApJ*, 616, 16
- González-García A. C., van Albada T. S., 2005a, *MNRAS*, 361, 1030
- González-García A. C., van Albada T. S., 2005b, *MNRAS*, 361, 1043
- Governato F., Mayer L., Wadsley J., Gardner J. P., Willman B., Hayashi E., Quinn T., Stadel J., Lake G., 2004, *ApJ*, 607, 688

- Guiderdoni B., Hivon E., Bouchet F. R., Maffei B., 1998, *MNRAS*, 295, 877
- Hearn N. C., Lamb S. A., 2001, *ApJ*, 551, 651
- Hernquist L., 1989, *Nature*, 340, 687
- Hernquist L., 1990, *ApJ*, 356, 359
- Hernquist L., 1992, *ApJ*, 400, 460
- Hernquist L., 1993a, *ApJS*, 86, 389
- Hernquist L., 1993b, *ApJ*, 404, 717
- Hernquist L., 1993c, *ApJ*, 409, 548
- Hernquist L., Spergel D. N., Heyl J. S., 1993, *ApJ*, 416, 415
- Hibbard J. E., Mihos J. C., 1995, *AJ*, 110, 140
- Hultman J., Pharasyn A., 1999, *A&A*, 347, 769
- Jonsson P., 2004, PhD thesis, UC Santa Cruz, <http://sunrise.familjenjonsson.org/thesis>
- Jonsson P., 2006, *astro-ph/0604118*
- Jonsson P., Cox T. J., Primack J. R., Somerville R. S., 2006, *ApJ*, 637, 255
- Joseph R. D., Wright G. S., 1985, *MNRAS*, 214, 87
- Katz N., 1992, *ApJ*, 391, 502
- Katz N., Weinberg D. H., Hernquist L., 1996, *ApJS*, 105, 19
- Kawata D., Gibson B. K., 2005, *MNRAS*, 358, L16
- Kay S. T., Pearce F. R., Frenk C. S., Jenkins A., 2002, *MNRAS*, 330, 113
- Kennicutt R. C., 1998, *ApJ*, 498, 541
- Kennicutt R. C., Roettiger K. A., Keel W. C., van der Hulst J. M., Hummel E., 1987, *AJ*, 93, 1011
- Khochfar S., Burkert A., 2006, *A&A*, 445, 403
- Kobayashi C., 2004, *MNRAS*, 347, 740
- Kravtsov A. V., 2003, *ApJL*, 590, L1
- Lamb S. A., Hearn N. C., Gao Y., 1998, *ApJL*, 499, L153+
- Lambas D. G., Tissera P. B., Alonso M. S., Coldwell G., 2003, *MNRAS*, 346, 1189
- Larson R. B., Tinsley B. M., 1978, *ApJ*, 219, 46
- Li Y., Mac Low M.-M., Klessen R. S., 2004, *ApJL*, 614, L29
- Li Y., Mac Low M.-M., Klessen R. S., 2005, *ApJ*, 626, 823
- Li Y., Mac Low M.-M., Klessen R. S., 2006, *ApJ*, 639, 879
- Marri S., White S. D. M., 2003, *MNRAS*, 345, 561
- Martin C. L., 1999, *ApJ*, 513, 156
- Martin C. L., 2005, *ApJ*, 621, 227
- Martin C. L., Kennicutt R. C., 2001, *ApJ*, 555, 301
- McDowell J. C., Clements D. L., Lamb S. A., Shaked S., Hearn N. C., Colina L., Mundell C., Borne K., Baker A. C., Arribas S., 2003, *ApJ*, 591, 154
- Mihos J. C., Bothun G. D., 1997, *ApJ*, 481, 741
- Mihos J. C., Hernquist L., 1994a, *ApJL*, 437, L47
- Mihos J. C., Hernquist L., 1994b, *ApJ*, 437, 611
- Mihos J. C., Hernquist L., 1994c, *ApJL*, 431, L9
- Mihos J. C., Hernquist L., 1996, *ApJ*, 464, 641
- Mihos J. C., Richstone D. O., Bothun G. D., 1991, *ApJ*, 377, 72
- Milosavljević M., Merritt D., 2001, *ApJ*, 563, 34
- Mo H. J., Mao S., White S. D. M., 1998, *MNRAS*, 295, 319
- Mosconi M. B., Tissera P. B., Lambas D. G., Cora S. A., 2001, *MNRAS*, 325, 34
- Naab T., Burkert A., 2003, *ApJ*, 597, 893
- Naab T., Trujillo I., 2005, *MNRAS* accepted (*astro-ph/0508362*)
- Navarro J. F., Frenk C. S., White S. D. M., 1997, *ApJ*, 490, 493
- Navarro J. F., White S. D. M., 1993, *MNRAS*, 265, 271
- Negroponte J., White S. D. M., 1983, *MNRAS*, 205, 1009
- Nikolic B., Cullen H., Alexander P., 2004, *MNRAS*, 355, 874
- Nipoti C., Londrillo P., Ciotti L., 2003, *MNRAS*, 342, 501
- Novak G. S., Cox T. J., Primack J. R., Jonsson P., Dekel A., 2006, *ApJL*, 646, L9
- Okamoto T., Eke V. R., Frenk C. S., Jenkins A., 2005, *MNRAS*, 363, 1299
- Padmanabhan N., Seljak U., Strauss M. A., Blanton M. R., Kauffmann G., Schlegel D. J., Tremonti C., Bahcall N. A., Bernardi M., Brinkmann J., Fukugita M., Ivezić Ž., 2004, *New Astronomy*, 9, 329
- Power C., Navarro J. F., Jenkins A., Frenk C. S., White S. D. M., Springel V., Stadel J., Quinn T., 2003, *MNRAS*, 338, 14
- Roberts M. S., Haynes M. P., 1994, *ARA&A*, 32, 115
- Robertson B., Cox T. J., Hernquist L., Franx M., Hopkins P. F., Martini P., Springel V., 2006, *ApJ*, 641, 21
- Robertson B., Yoshida N., Springel V., Hernquist L., 2004, *ApJ*, 606, 32
- Rothberg B., Joseph R. D., 2004, *AJ*, 128, 2098
- Rupke D. S., Veilleux S., Sanders D. B., 2002, *ApJ*, 570, 588
- Rupke D. S., Veilleux S., Sanders D. B., 2005, *ApJS*, 160, 115
- Salo H., Laurikainen E., 2000, *MNRAS*, 319, 377
- Sanders D. B., Mirabel I. F., 1996, *ARA&A*, 34, 749
- Scannapieco C., Tissera P. B., White S. D. M., Springel V., 2005, *MNRAS*, 364, 552
- Scannapieco C., Tissera P. B., White S. D. M., Springel V., 2006, *MNRAS*, pp 878+
- Schmidt M., 1959, *ApJ*, 129, 243
- Semelin B., Combes F., 2002, *A&A*, 388, 826
- Smith B. J., Struck C., Nowak M. A., 2005, *AJ*, 129, 1350
- Somerville R. S., Primack J. R., Faber S. M., 2001, *MNRAS*, 320, 504
- Sommer-Larsen J., Götz M., Portinari L., 2003, *ApJ*, 596, 47
- Springel V., 2000, *MNRAS*, 312, 859
- Springel V., 2005, *MNRAS*, 364, 1105
- Springel V., Di Matteo T., Hernquist L., 2005a, *ApJL*, 620, L79
- Springel V., Di Matteo T., Hernquist L., 2005b, *MNRAS*, 361, 776
- Springel V., Hernquist L., 2002, *MNRAS*, 333, 649
- Springel V., Hernquist L., 2003, *MNRAS*, 339, 289
- Springel V., Hernquist L., 2005, *ApJL*, 622, L9
- Springel V., White S. D. M., 1999, *MNRAS*, 307, 162
- Springel V., Yoshida N., White S. D. M., 2001, *New Astronomy*, 6, 79
- Stinson G., Seth A., Katz N., Wadsley J., Governato F., Quinn T., 2006, *MNRAS* submitted (*astro-ph/0602350*)
- Struck C., Kaufman M., Brinks E., Thomasson M., Elmegreen B. G., Meloy Elmegreen D., 2005, *MNRAS*, 364, 69
- Struck C., Smith B. J., 2003, *ApJ*, 589, 157
- Sutherland R. S., Dopita M. A., 1993, *ApJS*, 88, 253
- Thacker R. J., Couchman H. M. P., 2000, *ApJ*, 545, 728
- Thacker R. J., Couchman H. M. P., 2001, *ApJL*, 555, L17
- Thacker R. J., Tittley E. R., Pearce F. R., Couchman H. M. P., Thomas P. A., 2000, *MNRAS*, 319, 619

- Toomre A., 1977, in *Evolution of Galaxies and Stellar Populations Mergers and Some Consequences*. p. p.401
- Toomre A., 1981, in Fall S. M., Lynden-Bell D., eds, *Structure and Evolution of Normal Galaxies What amplifies the spirals*. pp 111–136
- Toomre A., Toomre J., 1972, *ApJ*, 178, 623
- Tornatore L., Borgani S., Matteucci F., Recchi S., Tozzi P., 2004, *MNRAS*, 349, L19
- Veilleux S., Kim D.-C., Sanders D. B., 2002, *ApJS*, 143, 315
- Veilleux S., Kim D.-C., Sanders D. B., Mazzarella J. M., Soifer B. T., 1995, *ApJS*, 98, 171
- Wong T., Blitz L., 2002, *ApJ*, 569, 157
- Wyithe J. S. B., Loeb A., 2003, *ApJ*, 595, 614
- Yepes G., Kates R., Khokhlov A., Klypin A., 1997, *MNRAS*, 284, 235